Overturning Instabilities Across a Warm Core Ring From Glider Observations

J. G. C. Pérez, E. Pallàs-Sanz, M. Tenreiro, T. Meunier, Julien Jouanno, A. Ruiz-Angulo

JGR Oceans

RESEARCH ARTICLE
10.1029/2021JC017527

Overturning Instabilities Across a Warm Core Ring From Glider Observations

J. G. C. Pérez[1], E. Pallàs-Sanz[1], M. Tenreiro[1], T. Meunier[2], J. Jouanno[3], and A. Ruiz-Angulo[4]

[1]Centro de Investigación Científica y de Educación Superior de Ensenada, Ensenada, Mexico, [2]Woods Hole Oceanographic Institution (WHOI), Woods Hole, MA, USA, [3]Laboratoire d'Etudes en Geophysique et Oceanographie Spatiales, Toulouse, France, [4]Institute of Earth Sciences, University of Iceland, Reykjavík, Iceland

Key Points:

- The core of the Warm Core Ring is more (less) susceptible to gravitational instabilities during winter (summer)
- Favorable conditions for symmetrically unstable mixed layer are captured by the glider observations during a down-front wind event
- At the periphery of Warm Core Ring, observations of negative potential vorticity suggest favorable conditions to symmetric instabilities

Supporting Information:

Supporting Information may be found in the online version of this article.

Correspondence to:

J. G. C. Pérez,
jcorrea@cicese.edu.mx

Citation:

Pérez, J. G. C., Pallàs-Sanz, E., Tenreiro, M., Meunier, T., Jouanno, J., & Ruiz-Angulo, A. (2022). Overturning instabilities across a Warm Core Ring from glider observations. *Journal of Geophysical Research: Oceans*, *127*, e2021JC017527. https://doi.org/10.1029/2021JC017527

Received 29 APR 2021
Accepted 11 MAR 2022

Abstract This work presents new evidence for conducive conditions for the existence of overturning instabilities in the mixed layer across a mesoscale anticyclonic Loop Current Eddy (LCE) and surrounding cyclonic eddies in the Gulf of Mexico (GoM). The LCE was intensively sampled using four gliders during 12 months. The LCE is characterized by a strong anomaly of fresh and warm water in the center and strong strain at the periphery. Mixed layers prone to overturning instabilities are diagnosed from the gradients of buoyancy. In the GoM, the reduction of potential vorticity (PV) in the mixed layer is driven by surface cooling by year-round persistent negative turbulent heat fluxes, eventually reaching -700 W m^{-2} during extreme winter wind events. Lateral buoyancy gradients associated with submesoscale filaments and fronts at the periphery of the LCE enhance the frictional torque supplied by the wind stress when aligned with the geostrophic jet current. Negative PV in the mixed layer occurs simultaneously with negative turbulent heat fluxes and events of Ekman buoyancy fluxes that reduce the stratification. These regions are susceptible to mixed-layer gravitational-symmetric instability preferentially in winter. Extreme Ekman equivalent heat flux ($\leq -10{,}000$ W m^{-2}) associated with wind stress of 1.2 N m^{-2} coincides with the development of inertial-symmetric instability across anticyclonic vorticity. These observations might have several implications for the restratification processes, kinetic energy budget, and biogeochemical cycles inside LCEs and can contribute to the formation of low-PV waters that could feed mode water formation inside the GoM.

Plain Language Summary Recent computational simulations of ocean circulation have shown intense vertical velocities associated with the so-called "submesoscale" currents as eddies, fronts, and filaments, occurring at horizontal scales of 1–10 km and life spans of 1 day. Fine-scale temperature and salinity measurements obtained using autonomous underwater vehicles, called gliders, in the Gulf of Mexico (GoM), are used to identify the times and locations where overturning instabilities modulate the ocean–atmosphere exchanges. These instabilities are enhanced inside eddies ubiquitous in the Gulf and at their periphery forced by strong winds during winter. A high-resolution model of the circulation of the GoM confirms the observations for contrasting wind conditions. These submesoscale diagnostics might be relevant to understand the transfer of kinetic energy from larger to smaller scales, the life cycle of eddies, and the vertical distribution of nutrients and biological activity in the sunlit upper ocean, which includes the atmospheric carbon dioxide sequestration.

1. Introduction

Overturning instabilities enhance the buoyancy exchange across frontal structures returning the flow to a stable state (Boccaletti et al., 2007; Callies et al., 2015; Fox-Kemper et al., 2008; McWilliams, 2016; Su et al., 2018; Yang et al., 2021). They can significantly modify the transfer of kinetic energy from the balanced flow to dissipative smaller scales (Capet et al., 2008a, 2008c; Poje et al., 2017; Zhang & Qiu, 2018). Submesoscale motions, such as submesoscale vortices, filaments, and fronts, have been intensively studied in the last decade thanks to the improvement in numerical models resolution. The submesoscale regime occurs at horizontal scales of hundred meters to several kilometers, vertical scales of 10–100 m, and temporal scales of hours to days (McWilliams, 2016). Numerical simulations at horizontal resolutions of $O(1)$ km revealed filamented-like flow structures with enhanced vertical velocities of $O(100)$ m day^{-1} and with both Rossby [U/fL] and Richardson [N^2H^2/U^2] numbers of $O(1)$ (Capet et al., 2008b; Mahadevan & Tandon, 2006), where U is the horizontal velocity scale, L and H are the horizontal and vertical length scales, respectively, f is the Coriolis frequency, $N^2 = \partial b/\partial z$ is the squared Brunt–Väisälä frequency, and $b = -g\rho/\rho_o$ is buoyancy (ρ is the density, $\rho_o = 1{,}025$ kg m^{-3} is a reference

density, and g is the gravitational acceleration). The vertical velocity at submesoscale is 1 order of magnitude larger than at the mesoscale (~10 m day^{-1}), which stresses the importance of submesoscale flow structures in modulating the vertical distribution of nutrients and primary production (Gaube et al., 2014) and enhancing the upper ocean vertical fluxes of buoyancy and potential vorticity (PV), hence, modifying the upper ocean stratification. Upper ocean submesoscale turbulence triggers an upward heat transport 5 times larger than mesoscale vertical transport and thus has important implications in global climate (Su et al., 2018).

High-resolution numerical simulations including Large Eddy Simulations have been used to study submesoscale phenomenology, such as: (i) dynamics of submesoscale filaments and vortices (Gula et al., 2014, 2015, 2019; Meunier, Tenreiro, et al., 2018), (ii) submesoscale instabilities and their effect on restratification of the upper ocean (Boccaletti et al., 2007; Fox-Kemper et al., 2008; Haine & Marshall, 1998; Mahadevan & Tandon, 2006; Mahadevan et al., 2010; Thomas et al., 2008; Taylor & Ferrari, 2010; Thomas & Taylor, 2010; Thomas et al., 2008), (iii) submesoscale frontogenesis (Barkan et al., 2019; Capet et al., 2008b; Lapeyre et al., 2006; McWilliams, 2017), and (iv) impact of submesoscale on primary productivity (Mahadevan, 2016). Special attention has been paid recently to the frictional modification of PV in the surface boundary layer (SBL) by the Ekman buoyancy flux (EBF) associated with wind stress (Mahadevan & Tandon, 2006; Thomas, 2005; Thomas & Lee, 2005) and the "geostrophic Ekman buoyancy flux" (EBF_g) driven by an effective "geostrophic stress" (Bachman & Taylor, 2016; Wenegrat et al., 2018 and Section 3.3) over submesoscale frontal structures. Most of these studies focus on the development of vertical overturning in the mixed layer at frontal regions driven by large-scale deformation fields, wind-driven Ekman flows, and the vertical mixing of momentum, but little is known about submesoscale instabilities over mesoscale eddying flows. Recent numerical efforts revealed intense submesoscale upwelling in anticyclonic eddies forming high-PV filaments into the mixed layer associated with symmetric instabilities (SIs), which grow faster in anticyclonic vorticity than in cyclonic (Brannigan, 2016; Brannigan et al., 2017). The authors show that the intensity of the submesoscale across a mesoscale eddy is related to frictional processes and it is much larger in regions of the eddy that have been exposed to down-front wind for a longer time, that is, wind stress blowing in the direction of the frontal geostrophic current. From an observational point of view, Adams et al. (2017) use high-resolution Seasoar conductivity–temperature–depth (CTD) data to show favorable conditions for SIs concentrated near lateral density gradients at the periphery of a mesoscale cyclonic eddy separated from the Antarctic Circumpolar Current.

In situ observations of submesoscale are challenging because of their small spatial scales and high frequencies, and because the variability at spatial scales below 30–40 km can be aliased due to propagation of high-frequency near-inertial gravity waves in the mixed layer related to the slowness of ocean sampling platforms and discrete sampling (Qiu et al., 2018; Rudnick & Cole, 2011). Improvements in instrument resolution and sampling techniques also yield an enhancement of the resolved Rossby numbers, vertical velocity, and vertical fluxes at submesoscale (Buckingham et al., 2016; Ohlmann et al., 2017; Shcherbina et al., 2013; J. Yu et al., 2018).

The literature clearly shows that the vertical buoyancy fluxes are significantly enhanced at submesoscale resolving resolutions. However, observations of the distribution and seasonality of the occurrence of overturning instabilities (thereby vertical buoyancy fluxes) across the mixed layer of mesoscale eddies are still largely unknown. Few studies have attempted to describe the seasonal cycle of submesoscale flows using in situ data. Callies et al. (2015), using high-resolution velocity and buoyancy transects in the Gulf Stream, found enhanced submesoscale activity in the deep winter mixed layers. Buckingham et al. (2016), using glider and mooring data in the North Atlantic, showed evidence of larger relative vorticity and a bias toward cyclonic values. To our knowledge, Thompson et al. (2016) and X. Yu et al. (2021) are the only observational studies that assessed the seasonal cycle of overturning instabilities using glider data and seasonal evolution of PV measured from mooring array over a small patch of 15 km × 15 km on the northern boundary of the North Atlantic anticyclonic gyre (OSMOSIS domain). Both works show deepening of the mixed layer through surface cooling and gravitational instabilities (GIs) during autumn that lead to background conditions favorable to SIs in winter that can reverse the sign of the equivalent heat fluxes and restratify the mixed layer. Oppositely, in spring and summer, stratification dominates and instabilities are notably inhibited. These results, however, are obtained from "Eulerian" glider observations and, hence, the instability diagnostics, based on horizontal buoyancy gradients, are associated with a wide range of flow structures that are advected across the OSMOSIS domain (i.e., fronts, eddies, and filaments).

Here, we implement existing methodologies to distinguish between the different natures of mixed-layer instabilities and the resulting equivalent heat fluxes across an anticyclonic mesoscale Loop Current Eddy (LCE) called

Poseidon. A fleet of four gliders operating in the western Gulf of Mexico (GoM) sampled Poseidon from August 2016 to August 2017, covering a full seasonal cycle. Poseidon is one of the largest LCEs observed in the GoM for the last 25 years in terms of size, heat and salt content, and sea surface height (Meunier, Pallàs-Sanz, et al., 2018; Meunier et al., 2020; Sosa-Gutiérrez et al., 2020). This data set offers the opportunity to shed some light on the seasonal cycle and horizontal distribution of the upper ocean overturning instabilities over the same mesoscale structure. Using glider observations, the overturning instabilities cannot be directly resolved, but rather the diagnostics shown in this manuscript identify the times and location across the LCE when the background conditions are susceptible to these instabilities.

This manuscript is organized in seven sections. The glider data and the methodology used to identify the forcing and environmental conditions that lead to overturning instabilities are described in Sections 2 and 3, respectively. The description of the seasonal variability of hydrography and derived quantities across the mesoscale LCE Poseidon is shown in Section 4. Observational and numerical diagnostics of the background environmental conditions that drive overturning instabilities within Poseidon and their spatial and temporal distributions are shown in Section 5 and 6, respectively. Finally, the results are discussed in Section 7 and conclusions summarized in Section 8.

2. Data

2.1. Glider Data

The data used in this study (pressure, temperature, salinity, and optical backscatter) were collected during four glider missions between August 2016 and August 2017, in the central and western GoM (Figure 1). The missions were designed to cross the LCE Poseidon twice (quasi-rectilinear transects of 200–600 km) typically along a SW-NW axis direction with the exception of mission 0004. During this mission, after performing a short transect from the periphery to the eddy's center of ∼200 km, the compass failed on 22 December and the glider started to drift with the current, though still performing spiraling dives through the water column.

The gliders used are Seaglider®, equipped with an unpumped Seabird CTD probe and optical WetLabs Eco Triplet sensor. Sensor precisions for conductivity, temperature, and salinity are $\delta C = 0.003$ S m^{-1}, $\delta T = 0.001$°C, and $\delta S = 0.0069$, respectively. The glider samples the water column from the surface down to 1,000 m depth irregularly, depending on the vertical velocity and sensor's sampling rate. The glider's averaged vertical velocity is 0.15 m s^{-1} and sensor's sampling rate for Seabird CT-Sail and Aanderaa Optode and WetLabs Eco Triplet is 0.15 and 0.1 Hz, respectively. The resulting averaged horizontal resolution is $\Delta x = 2.77$ km, while the averaged vertical resolution is $\Delta z = 0.68$ m (Figures 1a and 1d). Glider observations provide high-resolution vertical profiles of temperature and conductivity; however, it should be noted that the derived horizontal gradients of buoyancy might be associated with spatial, temporal, or mixed spatial–temporal variability as the glider moves through the westward propagating LCE Poseidon.

Salinity is computed from conductivity, temperature, and pressure using the EOS-80 equation of state (EOS-80; UNESCO 1981). Potential density σ_θ is derived from temperature and salinity using EOS-80. WetLabs Eco Triplet provides optical measurements at three different wavelengths. The optical backscatter (at 700 nm) might be considered as a "quasi-conservative" tracer to provide evidences of mass exchanges between the thermocline and the mixed layer. Backscatter is a proxy of biomass concentration insensitive to changes of pigment concentration (see for instance Behrenfeld & Boss, 2006). However, in the GoM and especially inside large Warm Core Rings, the depth of the chlorophyll maximum correlates with the 1,025.5 kg m^{-3} isopycnal (Pasqueron de Fommervault et al., 2017) which is typically within the thermocline while the mixed layer is mostly nonfluorescent (not shown). Hence, changes in backscatter within the mixed layer could be attributed to entrainment of cold thermocline water and along-track variability, rather than phytoplankton growth.

To compute along-track σ_θ-gradients, and geostrophic velocity $\left(\boldsymbol{u}_h^g\right)$ via thermal-wind balance, potential density data were interpolated onto a regular grid of 2 km × 5 m (horizontal × vertical) by averaging the vertical profiles at 5 m-bins and interpolating them linearly along a 2 km along-track grid. This methodology assumes that glider's dives are vertical and it reduces the smoothing effect observed on the buoyancy gradients by using large decorrelation scales for optimal interpolation (Barnes, 1994).

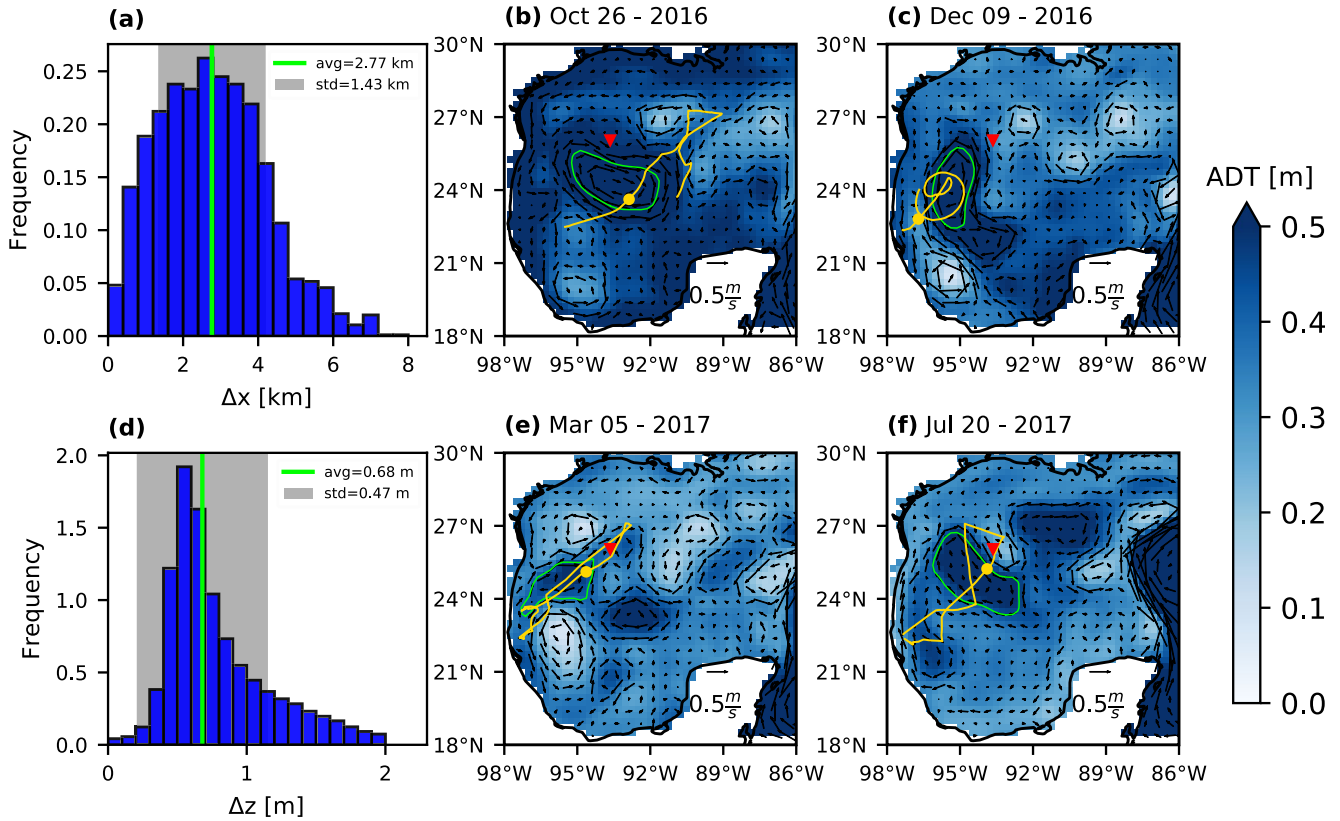

Figure 1. (a) Probability Density Functions (PDFs) of the horizontal profile separation (km) and (d) vertical resolution of measurements (m) for the four missions. Vertical green line is the mean and gray shading is the standard deviation. Absolute dynamic topography (ADT, m; colormap) and geostrophic velocity field ($\mathbf{U_g}$, m s^{-1}; black arrows) obtained from AVISO on (b) 26 October 2016 (mission 0003), (c) 9 December 2016 (mission 0004), (e) 5 March 2017 (mission 0005), and (f) 20 July 2017 (mission 0006). The green contours indicate the periphery of the Loop Current Eddy (LCE) Poseidon, for the dates shown in panels, computed using the algorithm implemented in Sosa-Gutiérrez et al. (2020). The yellow lines refer to glider tracks during each mission and the yellow dot is the glider position for each date (plus and cross markers indicate the beginning and ending locations of each glider mission). The red triangle refers to the location of the meteorological buoy 42002 of the National Data Buoy Center.

2.2. Satellite Data

2.2.1. Altimetry

We used AVISO daily absolute dynamic topography (ADT) and geostrophic currents ($\mathbf{U_g}$) covering the entire GoM for the period of measurements. Daily ADT helps the pilots to fly the gliders following a trajectory as much perpendicular to geostrophic velocity as possible. ADT is also used to detect the centroid and periphery of the LCE following Chaigneau et al. (2008) and modified in Sosa-Gutiérrez et al. (2020). The glider location relative to the center of the eddy or nondimensional radial coordinate is computed as $R_n = d/\mathcal{R}$, where d is the distance between glider location and eddy center and $\mathcal{R}$ is the eddy radius. Both $\mathcal{R}$ and the eddy center are provided by the detection algorithm of Chaigneau et al. (2008). The eddy edge is considered as the outermost closed ADT contour with the largest (along-contour) averaged azimuthal velocity. The eddy radius corresponds to the radius of an equivalent circular vortex having the same area delimited by eddy edge (Chaigneau et al., 2008).

Satellite-based ocean color is obtained from MODIS and distributed by the Ocean Biology Distributed Active Archive Center (OBDAAC). Daily sea surface temperature (SST) at 4 km horizontal resolution is obtained from MODIS and downloaded from NASA's Physical Oceanography Distributed Active Archive Center (PODAAC).

2.2.2. Ocean Heat Fluxes and Winds

Surface winds are produced by IFREMER and distributed by Copernicus Marine Environment Monitoring System (CMEMS; Belmonte Rivas & Stoffelen., 2019). The wind product is a blended satellite scatterometer

global 6-hourly averaged gridded fields of surface 10 m wind speed ($\mathbf{u_{10}}$) and wind stress ($\boldsymbol{\tau_h} = \tau_x\,\mathbf{i} + \tau_y\,\mathbf{j}$) with horizontal resolution of 0.25° × 0.25°. The air-sea heat fluxes is a gridded data set produced and distributed by IFREMER (Bentamy et al., 2013) and includes a blend of turbulent flux estimations on a spatial and temporal resolution of 0.25° × 0.25° and 24 hr, respectively. The determination of latent and sensible heat fluxes is based on the use of the European Space Agency (ESA) Ocean Heat Flux (OHF) project.

Hourly ERA5 (fifth generation ECMWF reanalysis for the global climate and weather) downward and upward radiative fluxes at surface (short and longwave radiative heat fluxes), interpolated on a regular grid of 0.25° × 0.25°, are obtained from COPERNICUS (Hersbach et al., 2020) and averaged daily.

2.3. National Data Buoy Center Buoys

Standard meteorological data ($\mathbf{u_{10}}$, SST, and air temperature) with 10-min temporal resolution were obtained from the National Data Buoy Center (NDBC). Wind and temperature data measured at the NDBC buoy 42002 (red triangles in Figure 1) are used to cross-validate with CMEMS gridded data and glider data, respectively. The data are further moving averaged using a 24hr-window.

3. Methods

3.1. Mixed-Layer and Convective Layer Depth

The mixed-layer depth (MLD) is computed using a density criteria as the depth at which the in situ density has increased by $\Delta\rho = 0.125$ kg m^{-3} from a near-surface value at 10 m depth (Kara et al., 2000). By choosing a density criteria, salinity variations associated with fresh water filaments within the mixed layer are taken into account. The convective layer depth (h_c) is introduced by Taylor and Ferrari (2010) and computed following Thomas et al. (2013):

$$\left(\frac{h_c}{H}\right)^4 - c^3\left(1 - \frac{h_c}{H}\right)^3\left(\frac{w_*^3}{|\Delta\mathbf{u}_h^g|^3} + \frac{u_*^2}{|\Delta\mathbf{u}_h^g|^2}\cos(\theta)\right)^2 = 0, \tag{1}$$

where $c \sim 14$ is an empirical constant, $w_* = (B_0 H)^{1/3}$ is the convective velocity scale (B_0 is the atmospheric buoyancy flux), $u^* = \sqrt{|\boldsymbol{\tau_h}|/\rho_o}$ is the friction velocity, $|\Delta\mathbf{u}_h^g|$ is the bulk difference in the geostrophic velocity across the low PV layer or SBL, and θ is the angle between the wind stress and the geostrophic shear vectors. The depth of the SBL (H) is defined as the upper ocean layer with PV lower than 10^{-9} s^{-3}.

3.2. Instability Criteria

Overturning instabilities occur when PV and planetary vorticity have opposite signs (see Equation B1). To distinguish between the different overturning instabilities (see also Appendix B), we use the instability angles (Thomas et al., 2013):

$$\phi_{Ri_b} = \tan^{-1}\left(-\frac{1}{Ri_b}\right) = \tan^{-1}\left(-\frac{|\overline{\nabla}_h b|^2}{f^2 N^2}\right) \tag{2}$$

and

$$\phi_c = \tan^{-1}\left(-\frac{\zeta^g}{f} - 1\right), \tag{3}$$

where $Ri_b = N^2/|\partial\mathbf{u}_h^g/\partial z|^2$ and $\zeta^g = \partial v^g/\partial x - \partial u^g/\partial y$ are the balanced Richardson number and the normalized geostrophic vertical vorticity, respectively, and $\mathbf{u}_h^g = u^g\,\mathbf{i} + v^g\,\mathbf{j}$ is the geostrophic velocity.

Depending on the source of kinetic energy that triggers the overturning instabilities, upright or slantwise convection might be expected to occur in the SBL. GIs derive their energy via surface buoyancy fluxes (unstable stratification). SIs extract kinetic energy mainly from geostrophic shear production. Inertial-symmetric instability (ISI) exists for stable stratification in anticyclonic vorticity and extracts energy from both, vertical shear of the balanced flow and its lateral shear (Thomas et al., 2013), while the mixed gravitational-symmetric instabilities

(GSIs) occur for unstable stratification and geostrophic shear production. The BCIs arise when $Ri_b \geq 1$ and can coexist with SIs for $Ri_b < 1$ (Haine & Marshall, 1998).

An equivalent methodology to identify GI-unstable mixed layers is to search for regions of unstable stratification, but ignoring the magnitude of the horizontal buoyancy gradients, using raw vertical density profiles (binned at 5 m depth intervals) and assuming that they are almost vertical within the mixed layer. Density inversions are identified as regions with $N^2 < -\delta N^2$, where

$$\delta N^2 = \frac{\sqrt{2}}{2\Delta z}\frac{g\delta\sigma_\theta}{\sigma_{\theta_o}} = 2\times 10^{-5}\ \mathrm{s}^{-2}, \tag{4}$$

is the accuracy of the estimated N^2 and $\delta\sigma_\theta$ is the standard deviation of potential density obtained by propagating the temperature and conductivity sensor precisions δC and δT, respectively, through the seawater equations. This filters out spurious density inversions due to sensor precision.

In situ PV (q_{gld}) and geostrophic vertical vorticity $\left(\zeta^g_{gld}\right)$ in this study are computed using the along-track buoyancy gradient and cross-track geostrophic velocity (v^g) as

$$q_{gld} = \underbrace{-\frac{1}{f}\left(\frac{\partial b}{\partial x}\right)^2}_{q_{bc}} + \underbrace{\left(f+\zeta^g_{gld}\right)N^2}_{q_{vert}} \tag{5}$$

and

$$\zeta^g_{gld} = \frac{\partial v^g}{\partial x}, \tag{6}$$

respectively, where for convenience we define the direction x as the along-track direction, regardless of the glider orientation. q_{bc} is related to geostrophic vertical shear through the thermal-wind relation and q_{vert} to geostrophic absolute vertical vorticity ($\zeta^g + f$) and vertical gradient of buoyancy. Cross-track geostrophic velocity is computed by vertically integrating the thermal-wind balance Equation A5 and using the depth-averaged velocity derived from the glider displacement through the water column as the reference velocity (Rudnick et al., 2015; Thompson et al., 2016; Meunier, Pallàs-Sanz, et al., 2018). Note that the accuracy of q_{gld} depends on the orientation of the glider track relative to the direction of the maximum thermohaline gradients; the error minimum (maximum) occurs when they are tangent (normal) (Thompson et al., 2016).

3.3. Equivalent Heat Fluxes

The vertical convection driven by overturning instabilities leads to equivalent heat fluxes that can restratify or deepen (mix) the SBL. Hereafter, we define positive (negative) heat fluxes as restratification (destratification) processes. Namely, the negative Ekman buoyancy fluxes $EBF = \mathbf{M}_e \cdot \nabla_h b < 0$ (i.e., down-front winds) are driven by the advection of dense water over light water across the front by the linear Ekman transport $\mathbf{M}_e = -(1/\rho_o f)\,\mathbf{k}\times\boldsymbol{\tau}_h$. In terms of equivalent heat flux, the EBF may be rewritten in the following form (Thompson et al., 2016; Viglione et al., 2018; note that Q_{Ek} has opposite sign than the EBF; throughout the manuscript, positive [negative] values of Q_{Ek} indicate increase [reduction] of stratification):

$$Q_{Ek} = -\frac{\boldsymbol{\tau}_y}{f}\frac{\partial b}{\partial x}\frac{C_p}{\alpha g}, \tag{7}$$

where α and C_p are the thermal expansion coefficient and specific heat capacity, respectively. Note that we have included a minus sign in the expression for Q_{Ek}, to indicate that the reduction of stratification occurs when Q_{Ek} is negative, being of opposite sign in theoretical PV fluxes shown in Appendix A.

The geostrophic Ekman buoyancy flux is $EBF_g = \mathbf{M}_{TTW}\cdot\nabla_h b$, where $\mathbf{M}_{TTW} = -(1/\rho_o f)\,\mathbf{k}\times\boldsymbol{\tau}^g_h \approx \left(\nu_E/f^2\right)\nabla_h b$ is the "turbulent thermal wind (TTW) transport" associated with geostrophic stress $\boldsymbol{\tau}^g_h = -\rho_o\nu_E\partial\mathbf{u}^g_h/\partial z$ at $z=0$ (Bachman & Taylor, 2016).

The eddy viscosity (ν_E) is parameterized as a function of the frictional velocity u^* and H ($\nu_E = 0.1Hu^*$; McWilliams, 2017; Wenegrat, 2018). Oppositely to Q_{Ek}, the geostrophic Ekman equivalent heat flux (Q_{TTW}) is directed down buoyancy gradient (advecting light water over dense water) and, thus, always restratify the SBL (Bachman & Taylor, 2016; his Equation 29) and can be written as follows:

$$Q_{TTW} = \frac{\nu_E}{f^2}\left(\frac{\partial b}{\partial x}\right)^2 \frac{\rho_o C_p}{\alpha g}. \tag{8}$$

Using the parameterization presented in Fox-Kemper et al. (2008), the equivalent heat flux associated with BCIs is

$$Q_{BCI} = 0.06\frac{H^2}{f}\left(\frac{\partial b}{\partial x}\right)^2 \frac{\rho_o C_p}{\alpha g}. \tag{9}$$

Q_{BCI} is always positive and has a restratifying effect.

3.4. Numerical Modeling

A moderately high-resolution numerical model of the GoM is used to assess the limitations of sampling horizontal gradients of a moving LCE with a slow-propagating glider. The numerical setup is based on a regional eddy-resolving configuration of the model Nucleus for European Modelling of the Ocean (NEMO, version 4.0; Madec, 2016). The configuration uses a grid of 1/108° ($\Delta x = \Delta y \sim 900$ m) encompassing the GoM and the Cayman Sea (from 98°W to 78°W and from 14°N to 31°N), with 75 vertical levels (including 12 levels in the upper 20 m and 24 levels in the upper 100 m). Temperature and salinity are advected using a Flux-corrected Transport (FCT) scheme with nearly horizontal diffusion parameterized as a Laplacian isopycnal diffusion. A "vector form" scheme is used for horizontal advection of momentum with diffusion computed with a bilaplacian operator and variable diffusion coefficient. The vertical diffusion coefficients are given by a Generic Length Scale (GLS) scheme with a k–ϵ turbulent closure Reffray et al. (2015). A logarithmic drag is applied at the bottom and no slip boundary conditions are applied at the lateral boundaries. The free-surface is solved using a time-splitting technique with the barotropic part of the dynamical equations integrated explicitly (Madec, 2016).

The model is forced at its lateral boundaries with daily means of high-resolution (1/12°) global Mercator Ocean reanalysis. The open boundary conditions radiate perturbations out of the domain and relax the model variables to 1-day averages of the reanalysis data. Details of the method are given in Madec (2016). At the surface, the atmospheric fluxes of momentum, heat, and freshwater are computed by bulk formulae using the COARE 3.5 algorithm (Edson et al., 2013). The model is forced with DFS5.2 product (Dussin et al., 2014) which is based on ERA-Interim reanalysis and consists in 3-hr fields of wind, atmospheric temperature and humidity, atmospheric pressure at the sea level, and daily fields of long, short wave radiation and precipitation. The shortwave radiation forcing is modulated on-line by a theoretical diurnal cycle. An interannual daily runoff based on the data set of ISBA-CTRIP (Decharme et al., 2019) is prescribed at the river mouths as a mass flux in the upper 10 m. The model is initialized using outputs from GLORYS12 at day 1 January 2009 and is integrated for 5 years. Hourly instantaneous outputs are used in this study from 11 to 18 December 2010 without overlapping the time period of glider observations.

4. Mesoscale LCE and Surrounding Cyclones

LCE Poseidon detached during spring 2016 and remained stationary in the eastern GoM until the end of August. The mean geostrophic Rossby numbers (ζ^g/f) computed from $\mathbf{U}_g$ (AVISO geostrophic currents) and using Equation 6 inside the mesoscale anticyclonic LCE are of the order of −0.1 (not shown). Geostrophic cyclonic vorticity ($\zeta^g > 0$) occurs at the periphery and surrounding cyclones, reaching values of similar magnitude. After ending the first section of the glider mission 0003, the LCE started to move westwards and the glider performed the second transect moving southwestwards. Poseidon reached the western shelf in December 2016 (mission 0004), where it interacted with the topography and other mesoscale eddies of the western GoM (missions 0005–0006).

The upper 200 m of the LCE is characterized by a bulge of warmer and fresher water contrasting with the surrounding Gulf Common Waters (GCWs; Figures 2a, 2b and C1) with both intense geostrophic velocity and

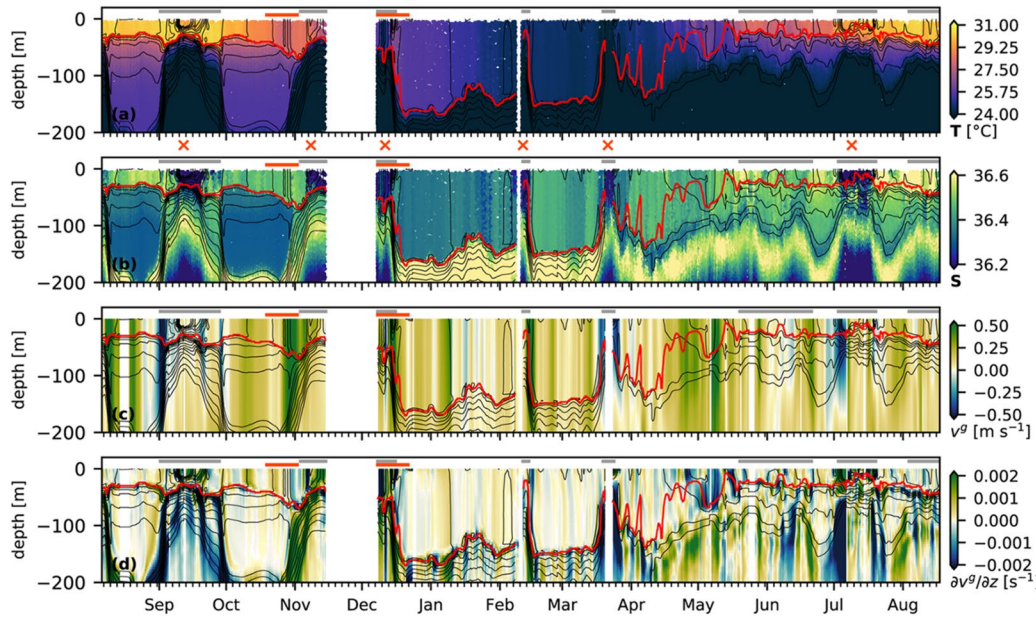

Figure 2. Time series of (a) temperature (T; °C) and (b) salinity (S) as measured by the glider's CT-sail, (c) derived (and interpolated) cross-track geostrophic velocity (v^g; m s^{-1}) and (d) geostrophic vertical shear ($\partial v^g/\partial z$; s^{-1}), as a function of depth. Red line indicates the mixed-layer depth. In the time series of temperature (a) and salinity (b), only every 12 data points are plotted. Horizontal gray and orange lines on top of the panels indicate regions of geostrophic cyclonic vorticity and the time span of the case study, respectively. Orange cross markers on top panel (b) refer to the times when fresh water filaments were sampled.

vertical shear within the main thermocline of the LCE (Figures 2c and 2d). Note that submesoscale structures with significant geostrophic vertical shear are found at the peripheries and inside the SBL of the LCE, although the largest values are found at the periphery. An example of submesoscale structures is the fresh water filaments (Figure 2b) advected around the LCE yielding strong thermohaline contrasts (Figure 2d).

The temperature and salinity in the mixed layer of the LCE follow a seasonal cycle with warmest (coldest) and saltier (fresher) waters in summer (winter), resulting in the formation of a shallow seasonal pycnocline in the summer months at ∼20 m (Figure 2a). During late autumn and winter, the seasonal pycnocline has been completely eroded and the mixed layer extends down to the base of the thermostat at ∼150 m depth. The high salinity core, signature of the North Atlantic Subtropical UnderWater (NASUW; Figure C1), is located within the main thermocline; below the thermostat in summer and below the deep mixed layer in winter (Figure 2b). The depth of the high salinity core is shallower in spring and summer 2017 suggesting erosion of NASUW during the decay of the LCE Poseidon. Transformation of NASUW to GCW is also evidenced in the temperature–salinity (T–S) diagram shown in Appendix C.

The in situ Ertel PV, q_{gld}, in the mixed layer is nearly zero, while in the seasonal and main thermocline, is largely positive (Figure 3). The term q_{vert} is by far the most important term contributing to PV, about 1–2 order of magnitude larger than the baroclinic term q_{bc} (not shown). Consequently, q_{gld} is governed by vertical stratification and follows a seasonal cycle in the mixed layer: high in summer ($q_{gld} > 10^{-9}$ s^{-3}) and low in winter ($\sim 10^{-10}$ s^{-3}). In late autumn and winter, q_{bc} can eventually dominate over q_{vert} and/or q_{vert} becomes negative (i.e., $N^2 < 0$) and, eventually, resulting in a sign-change q_{gld} within the mixed layer, providing favorable background conditions for the development of overturning instabilities, that is, $fq_{gld} < 0$ (Figure 3).

5. Diagnostics of Overturning Instabilities in the Mixed Layer

In the following section, we identify the times and locations of favorable conditions to overturning instabilities. They are diagnosed using the angles ϕ_{Ri_b} and ϕ_c (see Section 3.2). The %uML to a particular overturning instability is computed as the ratio between the fraction of the mixed layer unstable to overturning instabilities (Z_{uML}) and the MLD (multiplied by 100), that is, $\%uML = 100 Z_{\mathrm{uML}}/\mathrm{MLD}$. As indicated in Sections 2.1 and 3.2,

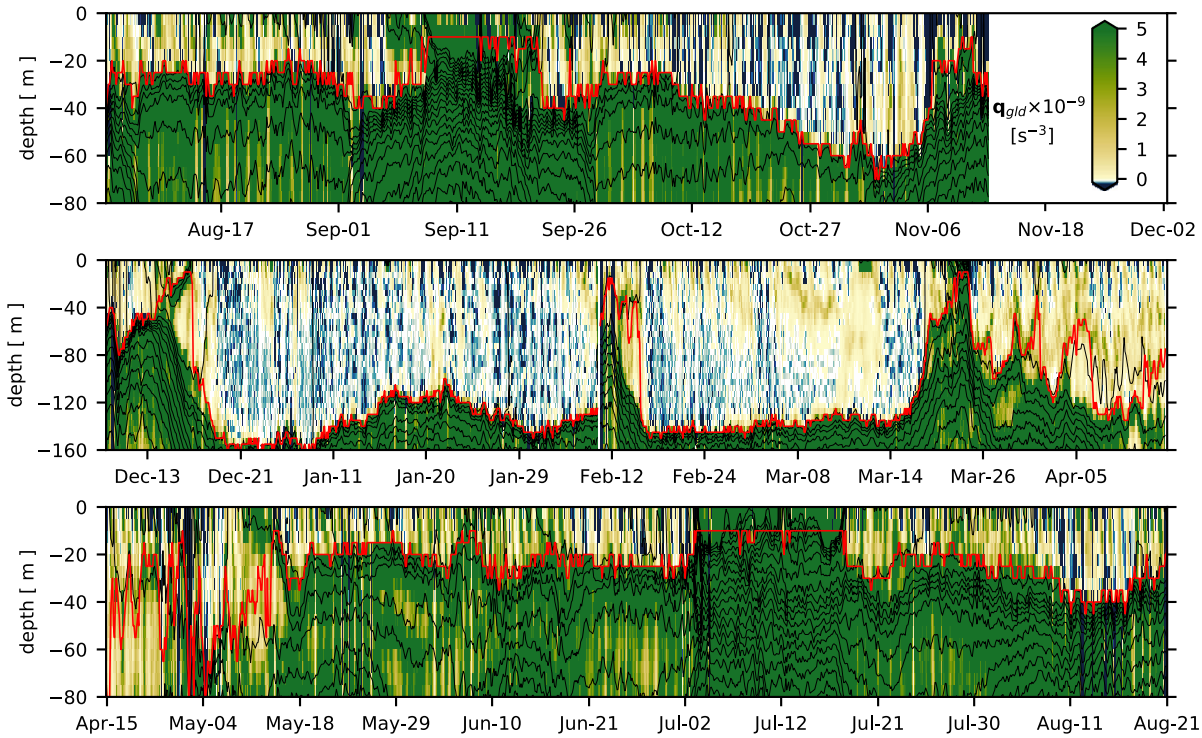

Figure 3. Along-track (time evolution) glider-derived Ertel potential vorticity (q_{gld}) as a function of depth. Red thick lines indicate the mixed-layer depth and black contours indicate density ($\Delta\rho = 0.1$ kg m^{-3}; minimum contour 1,023 kg m^{-3}). Note that the vertical and horizontal axis of the three panels is different.

instability angles are computed using the gridded 5 m × 2 km data and N^2-criteria using the raw 5 m-binned vertical profiles, respectively. The temporal evolution of the %uML to overturning instabilities (GIs, GSIs, SIs, and ISIs) and the distribution of the ϕ_{Ri_b} and regions of negative N^2-criteria as a function of time and depth are shown in Figures 4b–4d, respectively. As expected, we observed that overturning instabilities are confined in the mixed layer and a stable regime in the thermocline and below.

Despite that the dominant form of instabilities is the upright convection within the SBL, driven by strong atmospheric forcing that modulates the mixed layer over the entire synoptic basin, GIs cannot be considered as submesoscale process. In summer and early autumn, ϕ_{Ri_b} is typically larger then ϕ_c, consistent with stable mixed layer (Figures 4d and 4e; regions without color dots). Although the largest occurrence of GIs and GSIs inside the LCE is during winter, the mixed layer in summer and spring is also prone to GIs (Figures 3b and 3e; green shading and dots) and GSIs (Figures 3b and 3d; yellow shading and dots) in form of discrete and weaker convective events. The good agreement between regions with $-135 < \phi_{Ri_b} < -90$ and $N^2 < -2 \times 10^{-5}$ s^{-2} (Figures 4b, 4d and 4e) and the convective layers filling the depth of the SBL (Figure 4c; black line) suggests that GSIs are also expected in form of upright motions. In mid-autumn (15–31 October 2016), the deepening of the mixed layer and reduction of PV (Figure 3) lead to favorable conditions for the occurrence of overturning instabilities (Figures 4b–4d). This background preconditioning is enhanced during winter inside the LCE (Figure 3) until the SBL restratifies again suppressing the development of overturning instabilities (Figures 4b–4d).

The GSIs-unstable region $\left(-135° < \phi_{Ri_b} < -90°\right)$ inside the LCE during winter extends over large fraction of the mixed layer (80%; Figure 4b) and follows a similar trend than the GIs computed using the negative-N^2 criteria. The spatial correlation between regions with stable mixed layer (Figure 4d) and with the presence of filaments of high PV that extend from surface to the interior (Figure 3) suggests that near-surface submesoscale frontogenesis is active and inhibits the formation of GSIs favorable conditions in the upper ocean (Thomas et al., 2013). Overall, SIs and ISIs unstable water column $\left(-90° < \phi_{Ri_b} < \phi_c, for\, \zeta^g < 0\right)$ rarely exceeds 10% of the whole mixed layer (Figure 4c). However, at the LCE peripheries, eventually whole mixed layer becomes unstable to SIs and ISIs (Figure 4c). One example of large percentage of uML to ISIs occurs during the winter at the beginning of mission 0004 (8–22 December 2016) when the glider deployed on the western continental shelf started

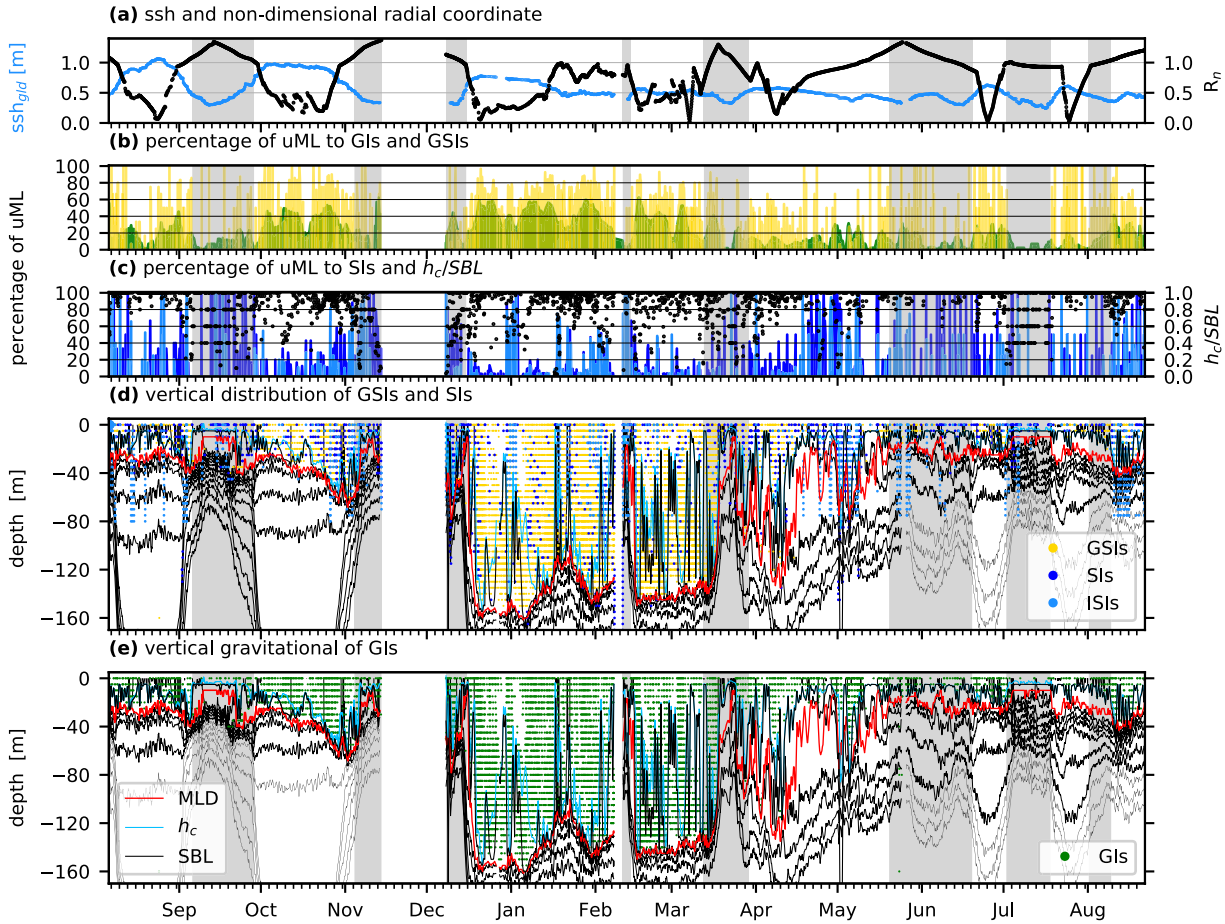

Figure 4. (a) Time series of the sea surface height interpolated along the glider trajectories (ssh$_{gld}$; m) shown in Figures 1b, 1c, 1e and 1f (blue line) and the nondimensional radial coordinate R$_n$ (black line). Percentage of unstable mixed layer (uML) to (b) mixed gravitational-symmetric instabilities (GSIs; yellow shading) and gravitational instabilities (GIs; green shading) diagnosed as density inversions with $N^2 < -2 \times 10^{-5}$ s^{-2}, (c) symmetric and inertial instabilities (SIs–ISIs; blue and light-blue lines, respectively) and superimposed the ratio h_c/H (black line). (d) Distribution of the meaningful ranges of ϕ_{Ri_b} for each type of instability: $-90° < \phi_{Ri_b} < -45°$ (SIs; blue dots), $-45° < \phi_{Ri_b} < \phi_c$ (ISIs; light-blue dots), and $-135° < \phi_{Ri_b} < -90°$ (GSIs; yellow dots). (e) Distribution of GIs as a function of depth and time. The depth of the convective layer (h_c; blue) and surface boundary layer (H; black) are included in panels (d) and (e). In this and subsequent figures, gray shading represent regions of cyclonic vertical vorticity as computed from satellite-derived surface geostrophic velocity interpolated along the glider trajectory.

to move northeastwards across a coastal upwelling front (see Figure S1) and the anticyclonic side of a filament (Figure 1c). Further details on the submesoscale diagnostics of the case study is shown in Section 5.3.

5.1. Equivalent Heat Fluxes

The reduction of PV in the mixed layer is largely driven by frictional and diabatic heat fluxes at the sea surface and is known to play an important role in triggering surface cooling and SIs (E. A. D'Asaro et al., 2018; Haine & Marshall, 1998; Marshall & Nurser, 1992; Taylor & Ferrari, 2010; Thomas, 2005; Thomas & Lee, 2005; Thomas et al., 2013). The winds from E-SE (i.e., *trade* winds) are prevailing in spring/summer, they are warm and wet, and can reach magnitudes up to $|\boldsymbol{\tau}_h| = 0.2$ N m^{-2} (Figure 5a). During autumn and winter months, intermittent atmospheric cold fronts cross the western GoM from NW to SE, that is, Northerly winds (Zavala-Hidalgo et al., 2014). These winds are dry and cold and drive surface stresses that are much stronger than the *trade* winds (Figures 5b and 5c). Several strong wind events occurred in winter, reaching maximum wind stress between 0.2 and 0.5 N m^{-2} at the location of the Northern NDBC buoy (Figure 5b). CMEMS wind stress interpolated at the glider track (τ_{gld}) during the Northerly events is 2–3 times larger than that measured at the Northern NDBC buoy because the glider at those times was located several tens of kilometers away from the NDBC buoy and near the western continental shelf, where winds are typically stronger (Luna-Niño & Cavazos, 2018). Northerly winds in

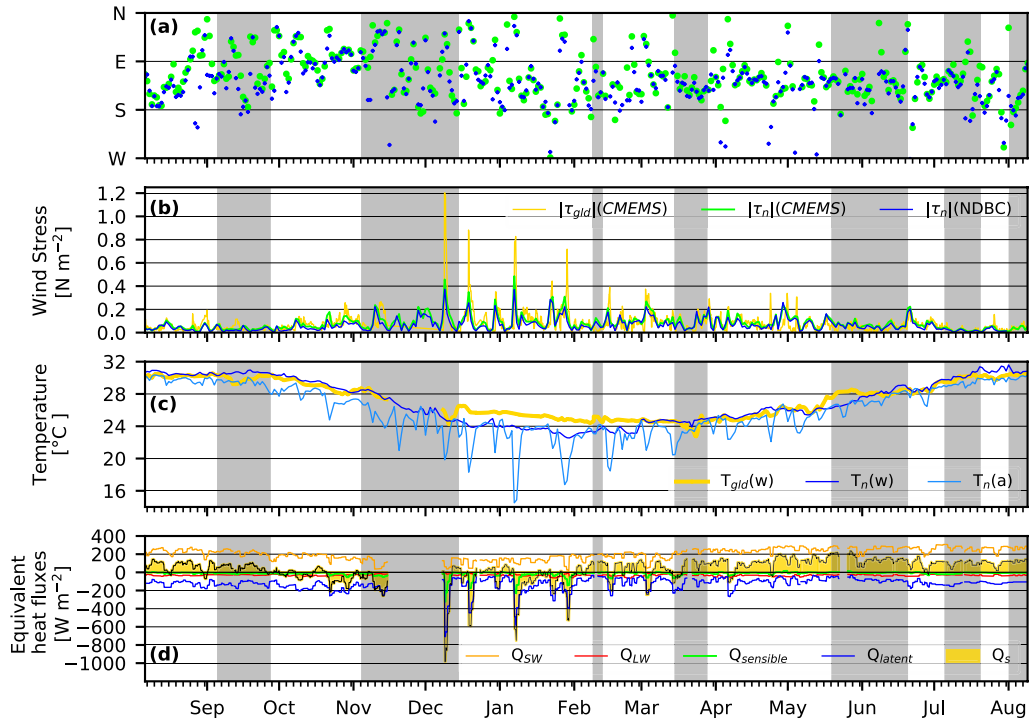

Figure 5. Atmospheric forcing: (a) wind direction and (b) wind stress (N m^{-2}) for Copernicus Marine Environment Monitoring System (CMEMS) reanalysis interpolated at the Northern National Data Buoy Center (NDBC) buoy (τ_n(CMEMS); light green line), for CMEMS reanalysis interpolated at the glider's track ($\tau_{gld}(CMEMS)$; yellow), and for the Northern NDBC buoy (τ_n(NDBC); dark blue line), (c) sea surface ($T_n(w)$; dark blue line) and air ($T_n(a)$; light-blue line) temperature (°C) measured at the Northern NDBC buoy and sea surface temperature at 2 m depth observed by the glider ($T_{gld}(w)$), and (d) equivalent heat fluxes (W m^{-2}): IFREMER latent Q_{latent} (dark blue line) and sensible $Q_{sensible}$ (light green line), ERA-Interim radiative, downward shortwave Q_{SW} (orange line) and upward longwave Q_{LW} (red line), and net heat flux Q_{surf} (yellow shading; black line).

winter drive strong atmosphere–ocean temperature contrasts of about [4–8]°C and enhanced latent heat fluxes compared to the yearly average (Figures 5c and 5d). Radiative heat fluxes are dominated by downward shortwave radiation ($Q_{SW} \gg Q_{LW}$) warming the upper GoM. Q_{SW} is modulated seasonally reaching maxima in summer/spring ([200–300] W m^{-2}) and minima in autumn/winter ([100–150] W m^{-2}). Negative latent heat fluxes in autumn/winter oppose Q_{SW} driving negative net surface heat fluxes (Figure 5d). Hereafter, CMEMS winds are used to compute the wind stress along the glider track, via linear interpolation, to diagnose wind-driven buoyancy fluxes in the SBL.

The total equivalent heat flux, $Q_{total} = Q_{Ek} + Q_{TTW} + Q_{BCI} + Q_s$, follows a similar seasonal trend as Q_s with larger negative values in winter than summer. The submesoscale equivalent heat fluxes (Q_{Ek}, Q_{TTW}, and Q_{BCI}) take relevance associated with both strong Northerly winds and strong buoyancy gradients across fresh water filaments at the periphery of the LCE, being up to 5 times larger than the atmospheric surface equivalent heat fluxes (Q_s) during specific wind events (Figure 6).

The Ekman equivalent heat flux reduces (increases) the q_{gld} in the SBL for down-front (up-front) winds. $Q_{Ek} < 0$ reduces the stratification in the SBL by Ekman transport of buoyancy from the dense to light side of the front and vice versa for restratifying $Q_{Ek} > 0$. During winter, both types of conditions occur and Q_{Ek} is negative (positive) in 8 (7) strong wind events (Table 1 and Figure 6). Notice that q_{gld} takes the largest negative values in the SBL when both, Q_{Ek} and Q_s, work together to extract q_{gld} out of the SBL, giving rise to overturning instabilities; the strongest negative Q_{Ek} occurred on 9 December associated with the strongest Northerly wind event of the year (Figures 5a and 5b). Furthermore, enhanced negative turbulent heat fluxes during extreme wind events (Figure 5d) prevail over positive Q_{Ek} for up-front conditions, still driving negative Q_{total} (Figure 6). During spring and summer (mid-March to early June 2017), positive $Q_{Ek} > 0$ (i.e., up-front winds) dominates the Q_{total} injecting PV into the SBL and restratifying.

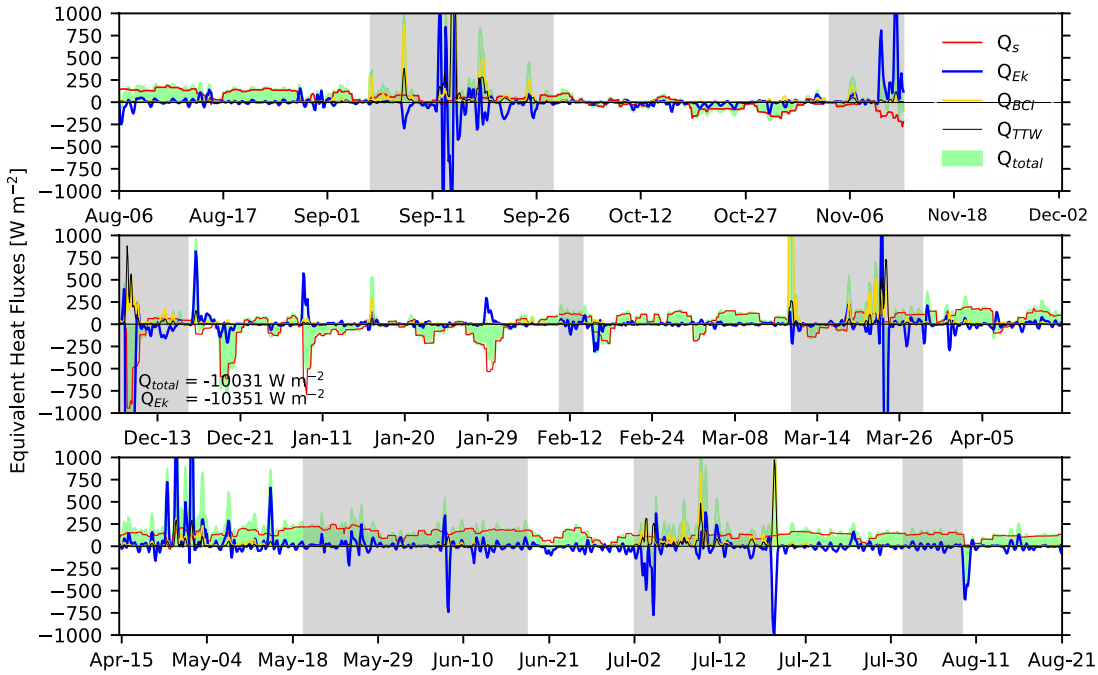

Figure 6. Ekman equivalent heat flux (Q_{Ek}; blue line), geostrophic Ekman equivalent heat flux (Q_{TTW}; black line), equivalent heat flux due to *BCI* (Q_{BCI}; yellow line), IFREMER surface equivalent heat flux (Q_s; red line), and total equivalent heat flux ($Q_{total} = Q_{Ek} + Q_{TTW} + Q_{BCI} + Q_s$; light green shading) in W m^{-2}.

Equivalent heat fluxes from baroclinic instability, Q_{BCI}, are largest at the periphery of the LCE, driven by buoyancy gradients associated with frontal structures including fresh water filaments advected offshore by the mesoscale flow (Figures 2 and 6). Finally, the restratifying equivalent heat fluxes due to cross-front advection by the TTW flow, Q_{TTW}, are similar to Q_{BCI} (Figure 6) as already pointed out in Wenegrat et al. (2018). We refer the

Table 1
Wind Events During the Year of Measurements ($|\tau_{gld}| > 0.25$ N m^{-2}): Wind Event #ID, Date, AVISO Geostrophic Current Direction (DirC; Degrees Clockwise From True North), CMEMS Wind Stress Direction (DirW; Degrees Clockwise From True North), CMEMS Wind Stress Magnitude ($|\tau_{gld}(CMEMS)|$; N m^{-2}), Nondimensional Radial Coordinate (R_n), Q_{Ek}, and Q_s (W m^{-2}), and Buoyancy Transformation ($q_{gld} < 0$ Refers to Mixing and $q_{gld} > 0$ to Restratifying Effect)

#ID	Date	DirC	DirW	$\lvert\tau_{gld}(CMEMS)\rvert_{max}$	R_n	$[Q_{Ek}]_{max}$	$[Q_s]_{max}$	Buoyancy
1	28 Oct 2016	272	220	0.28	0.74	−123	−110	Mixing
2	12 Nov 2016	315	182	0.26	1.20	1,425	−209	Restratify
3	9 Dec 2016	177	153	1.2	1.12	−10,351	−982	Mixing
4	19 Dec 2016	256	225	0.88	0.80	−208	−583	Mixing
5	30 Dec 2016	157	235	0.35	0.25	−63	−104	Mixing
6	7 Jan 2017	358	144	0.76	0.33	572	−625	Neutral
7	22 Jan 2017	146	166	0.36	0.90	−31	−148	Mixing
8	28 Jan 2017	248	183	0.54	0.78	296	−524	Neutral
9	16 Feb 2017	194	169	0.39	0.46	−85	−193	Mixing
10	3 Mar 2017	358	234	0.35	0.47	51	−247	Mixing
11	16 Mar 2017	−12	128	0.11	0.90	35	−75	Mixing
12	29 Mar 2017	83	315	0.30	0.74	212	93	Restratify
13	23 Apr 2017	20	170	0.30	0.83	723	−30	Restratify
14	2 Jul 2017	74	330	0.05	0.99	−215	118	Mixing
15	18 Jul 2017	304	299	0.04	0.92	−1,012	76	Mixing

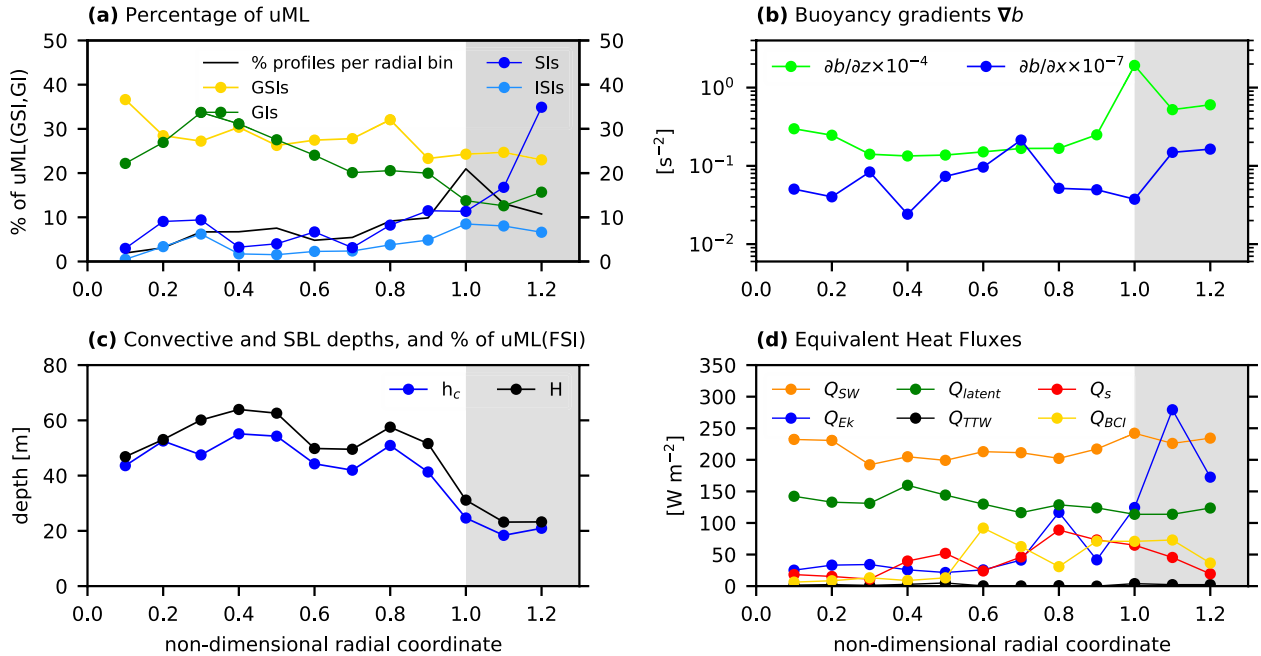

Figure 7. Radial composites of (a) percentage of the uML to overturning instabilities (yellow, green, blue, and light-blue lines) and the percentage of data used to construct the composites (for a total length record of 3,105 glider vertical profiles; black line), (b) along-track and vertical buoyancy gradients ($\partial b/\partial x$ and $\partial b/\partial z$, s^{-2}), (c) the convective layer depth (h_c, m; dark blue line), the depth of the SBL (H, m; black line), and (d) equivalent heat fluxes (see Section 3) computed using in situ glider measurements in W m^{-2}. Gray shading indicates geostrophic cyclonic vertical vorticity diagnosed as $\zeta^g/f > 0$, computed from satellite-derived AVISO geostrophic velocity.

reader to Appendix A for a detailed analysis of the relative strength between the different scalings for the vertical buoyancy fluxes. We anticipate that the atmospheric buoyancy flux inside the LCE is about 1–3 orders of magnitude larger than both EBF and EBF_g, while at the LCE periphery the frictional processes have similar importance than diabatic processes or even dominate them (see Appendix A).

5.2. Submesoscale Diagnostics in an Eddy-Centric Frame of Reference

To distinguish between the different regions unstable to overturning instabilities across the LCE, we have computed an eddy composite for the percentage of uML to overturning instabilities, buoyancy gradients, convective layer depth and the depth of the SBL, and the equivalent heat fluxes as a function of the nondimensional radial coordinate (Figure 7).

The glider was located near the periphery of the LCE more often (~20%) than in the eddy interior (~7%; black line in Figure 7a). Two relative maxima of the percentage of the uML to GSIs are located in the eddy's interior ($R_n \approx 0.1$) and near the periphery at $R_n \approx 0.8$ ([20–25]%). The percentage of the uML to GIs is maximum in the eddy's interior (32%; $R_n \simeq 0.3$) and rapidly decreases reaching ~10% at $R_n = 1.1$, similarly to the %uML to GSIs. Overall, the percentage of the SI-unstable (GSIs/GIs-unstable) mixed layer increases (decreases) from the eddy center toward the periphery, reaching an absolute maximum at $R_n \simeq 1.2$ ($R_n \simeq 1.1$).

Outside the eddy, cyclonic vorticity (Figures 1 and 4) is associated with smaller cyclonic eddies. The mixed layer is shallower and the horizontal gradients of buoyancy are larger at the periphery than inside the eddy (Figure 7b), reducing the APE in the mixed layer and providing a range for ϕ_{Ri_b} favorable to SI $\left(\phi_{Ri_b} > -90°\right)$, respectively. This preference for SIs to develop at the periphery is supported by the largest values of Q_{Ek} there (Figure 7d). Overall, the ISIs are few persistent inside the mixed layer across the entire LCE section ($\%uML$ to $ISIs < 10\%$), even if the lateral buoyancy gradients increase toward the periphery of the eddy.

Inside the LCE, the depth of the SBL is slightly deeper (~10 m) than the convective layer depth (Figure 7c) suggesting that convection dominates over SIs across the LCE because $h_c/H \simeq 1$ (Thomas et al., 2013). Some exceptions occur at the periphery of the LCE where $hc/H < 1$ (Figure 7c) and the %uML to SIs increase up to 30%

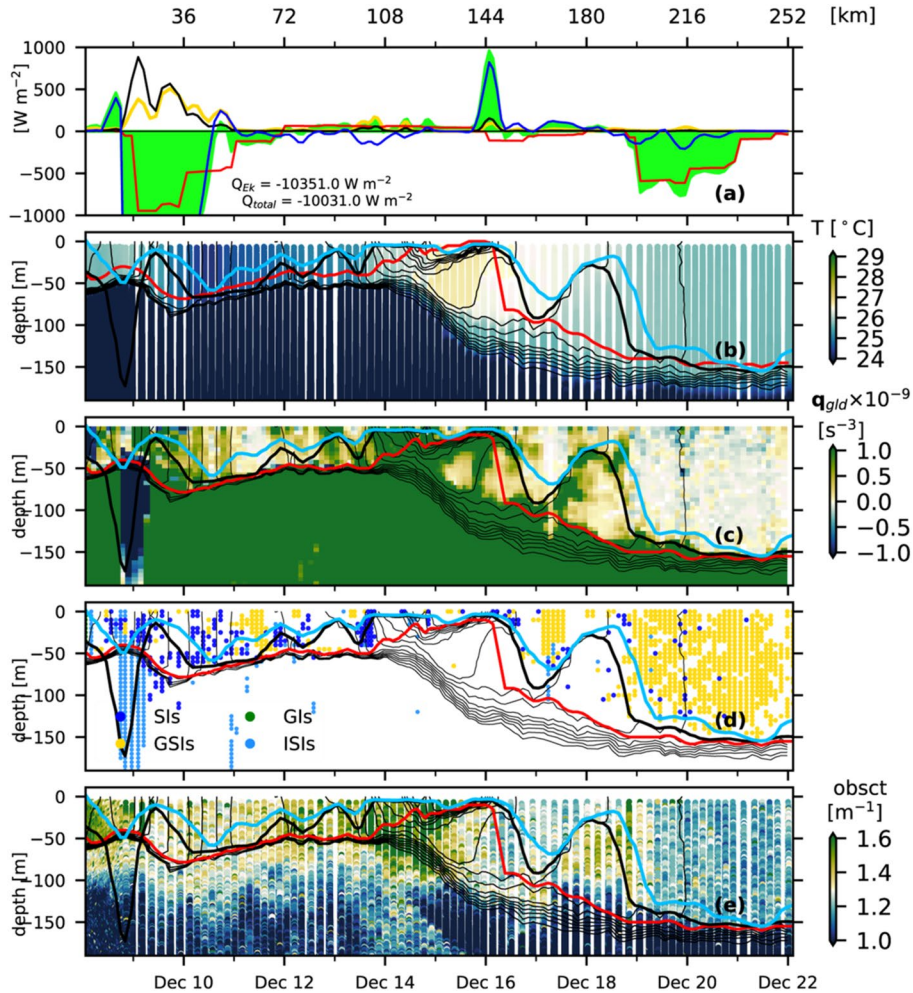

Figure 8. Diagnostics of overturning instabilities for the winter case study: (a) equivalent heat fluxes Q_{BCI}, Q_s, Q_{TTW}, Q_{Ek}, and the total $Q_{total} = Q_{BCI} + Q_s + Q_{TTW} + Q_{Ek}$ in W m^{-2}, Ertel vertical sections of (b) in situ temperature (T; °C), (c) glider-derived Ertel potential vorticity (q_{gld}; s^{-3}), (d) meaningful ranges of ϕ_{Ri_b} for each type of instability (GSIs for $-135° < \phi_{Ri_b} < -90°$; SIs for $-90 < \phi_{Ri_b} < -45°$; ISIs for $-45 < \phi_{Ri_b} < \phi_c$; and GIs for $N^2 < -2 \times 10^{-5}$ s^{-2} using raw (2 m-binned) sawtooth vertical profiles of density), and (e) glider's optical backscatter (obsct; m^{-1}) as a function of depth and time. All vertical sections depict the isopycnals (thin black lines; $\Delta\rho = 0.02$ kg m^{-3}), the depth of the convective layer (h_c; blue), and the depth of the surface boundary layer (H; black).

(Figure 7a). These instabilities based on negative PV-criteria can only be captured using glider observations if the front is crossed simultaneously during or just after a down-front wind event (see section below).

5.3. Case Study of SIs

Strong negative PV in the mixed layer was detected at the beginning of mission 0004. Figure 8 shows an example of ISIs and SI during winter across an unstable upwelling front at the western shelf of the GoM (see Figure S1). A cold filament is formed on the Western shelf by straining of the LCE and contracted it against the shelf (Figures 1c and 8b). In addition to the filament, the LCE also wrapped a light (fresh and warm) river plume around its periphery (Figures 2a, 2b and 8b), highlighting the richness on submesoscale structures of this region. Two down-front events associated with Northerly winds occur between 9–10 and 19–20 December 2016 (Figure 8a). The first is the largest wind event of the year and yields an Ekman equivalent heat flux of $Q_{Ek} = -10{,}351$ W m^{-2}, about 10 times larger than turbulent heat fluxes ($\simeq -982$ W m^{-2}). Q_{BCI} and Q_{TTW} are positive (restratifying) at the front but they are not sufficiently large to overcome the mixing effect of the cooling ($Q_s < 0$) and down-front wind ($Q_{Ek} < 0$). As a result, frictional destruction of PV deepens the SBL down to 210 m depth (Figure 8c) in presence

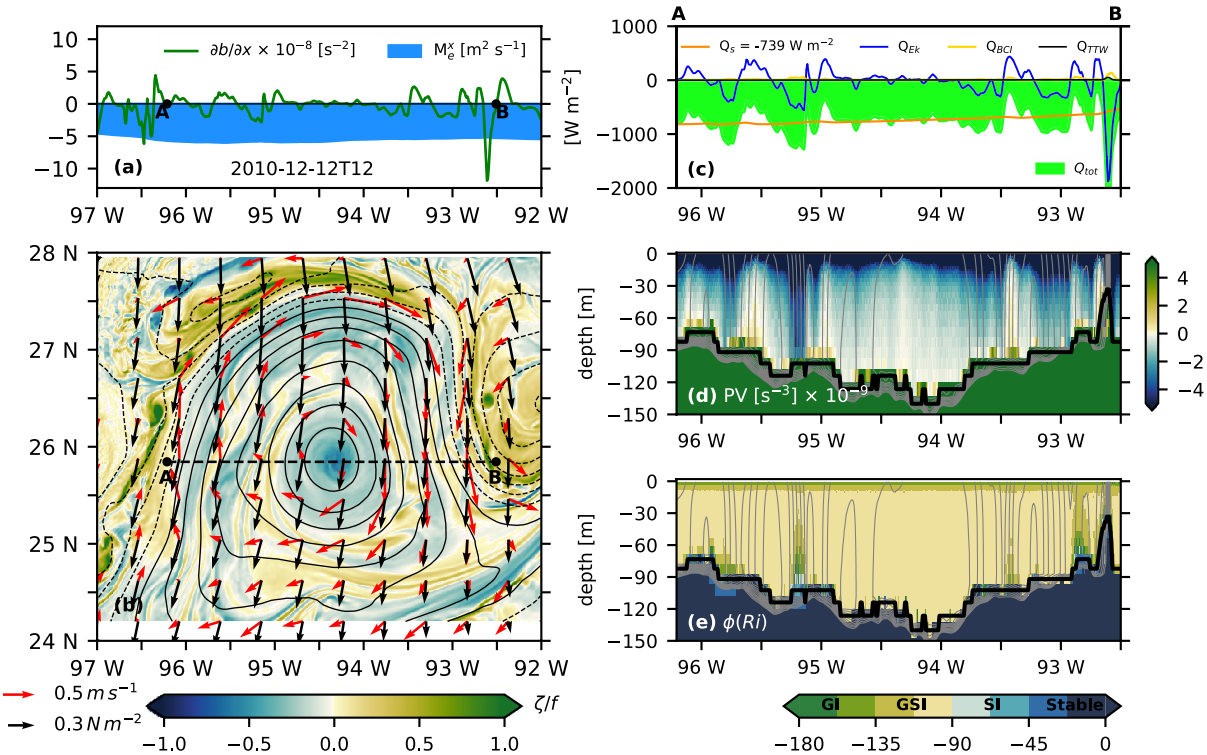

Figure 9. Diagnostics of overturning instabilities computed from model outputs for a Northerly wind event across a LCE: (a) Zonal Ekman transport M_e^x ($m^2\ s^{-1}$, blue shading; negative indicates transport westwards) and zonal buoyancy gradient $\partial b/\partial x$ (s^{-2}, dark green line) along the section **AB** shown in panel (b). (b) Horizontal distribution of vertical vorticity normalized by f (ζ/f; colormap), superimposed surface wind stress (N m^{-2}; black arrows), surface currents (m s^{-1}; red arrows), and sea surface height (m; black contours, Δ contour of 0.1 m). (c) Equivalent heat fluxes at the sea surface Q_s (orange line), $Q_{Ek} = \rho_o C_p / \alpha g \mathbf{M}_e \cdot \nabla_h b$ (blue line), Q_{TTW} (black line), Q_{BCI} (yellow line), and $Q_{total} = Q_s + Q_{TTW} + Q_{BCI} + Q_{Ek}$ (light green shading) in W m^{-2}. (d, e) Correspond to the vertical sections of AB for PV and ϕ_{Ri}, respectively. Thick black line defines the MLD and thin gray lines are isopycnals ($\Delta\rho = 0.02$ kg m^{-3}).

of anticyclonic vorticity and leads to favorable conditions for ISIs (Figure 8c). Temperature and optical backscatter (Figures 8b and 8e) decrease right after the occurrence of the SI on 10 December together with a deepening of the isopycnals (and mixed layer) consistent with the subduction of low PV at the center of the filament (see Figures 2c and 2d on 8–12 December). The large negative anomaly of PV on the western anticyclonic flank of the filament and the nearly zero PV in the center of the filament (Figure 8c), the larger MLD in the center of the filament (Figure 8b), and alternating anticyclonic and cyclonic circulation (Figures 1c and 2c) strongly suggest the presence of a cold filament. The reduced optical backscatter and the larger MLD in the center of the filament also suggest active mixing (Figures 8c and 8e) as parcels are transported across the filament and downwell into the thermocline (Gula et al., 2014).

The Northerly wind event on 19 December occurs when the glider is inside the LCE and within a deeper winter mixed layer ($MLD \simeq 160$ m). For this case, the destratifying joint effect of surface heat fluxes $Q_s + Q_{Ek} < 0$ is weaker ($\simeq -790$ W m^{-2}) than previous case study ($\simeq -11{,}351$ W m^{-2}). The PV reduction through a deeper mixed layer is also weaker and most of the mixed layer is now unstable to GSIs (Figure 8d).

6. Numerical Diagnostics of Overturning Instabilities

Because of the potential lack of synopticity of the glider measurements inherent to sampling LCEs and submesoscale structures with a slow-moving platform, we performed the same diagnostics shown in Section 5 using modeled density and velocity data. This analysis also provides insights on the validity of the approximate PV computed using the along-track glider measurements (q_{gld}). Figure 9 shows a mesoscale anticyclonic eddy located in the western GoM under the influence of Northerly cold winds. The time evolution of a whole Northerly and *Southerly* wind events is presented in the supporting information (see gif Figure S2).

The modeled LCE is visualized as a bulge of anticyclonic vertical vorticity (Figure 9b). Submesoscale filaments of alternating positive and negative vertical vorticity develop inside the LCE at 1 km model resolution. These submesoscale filaments inside the LCE are streamwise-aligned and are stacked in the radial direction, with wave phase lines not necessarily following isopleths of sea surface height and wrapping into the core of the LCE as shown in Brannigan et al. (2017). A thicker submesoscale filament with cyclonic vertical vorticity from the western coast is advected anticyclonically around the periphery of the LCE. The vertical section of PV across the numerical LCE is shown in Figure 9d. The core of the LCE is identified as a low-density anomaly and well-mixed PV layer of about 100 m; while at the periphery, the MLD shallows and the both stratification and PV increase significantly. These vertical distributions of density and PV across this LCE are in close agreement with the observations of the LCE obtained with gliders (Figure 3).

Across the LCE, alternating occurrence of Q_{Ek} positive and negative occurs at fronts/filaments observed as stacked vertical isopycnals (Figures 9c and 9d). Reduction of the PV in the mixed layer occurs for $\partial b/\partial x < 0$ and Northerly winds, that is, $M_e^x < 0$ (Figures 9a and 9d), and vice versa for *Southerly* winds (see gif Figure S2). Negative Q_s (-900 W m^{-2}) across the eddy extracts PV from the upper ocean, while Q_{Ek} has a large destratifying effect at large lateral buoyancy gradients $\partial b/\partial x$, that is, filaments, during down-front wind events, reversing the sign of the PV through the whole mixed layer (Figures 9c and 9d). For up-front winds ($Q_{Ek} > 0$) at the filaments, high PV from the thermocline is advected into the mixed layer (white-yellowish colors in Figure 9d).

The vertical distributions of modeled and observed ϕ_{Ri_b} across the LCE are similar (Figures 4d and 9e), that is, GSIs extending down to the base of the mixed layer. The uppermost water column (5–10 m) of the numerical LCE is gravitationally unstable which is in agreement with strong density inversions observed in the same depth range using glider data and a more restrictive criteria of $N^2 < -3 \times 10^{-3}$ s^{-2} (not shown). Around the filaments inside the eddy, SIs and GIs arise near the base of the mixed layer during down-front wind events.

7. Discussion

This work aims to characterize the overturning instabilities across a Warm Core Ring in the GoM using high-resolution (~2.7 km) in situ data obtained from four glider missions between August 2016 and August 2017. Complimentary, a moderately high-resolution (1/108°) regional numerical simulation of the GoM is also used.

Marginally stable PV inside the LCE ($PV \simeq 0$; Figure 3) provides favorable conditions for overturning instabilities to occur. Negative latent and sensible surface heat fluxes occur year round (Figure 5). Turbulent heat fluxes of $O(Q_{latent} + Q_{sensible}) \simeq -100$ W m^{-2} during summer and spring are largely canceled out by radiative equivalent heat fluxes of $O(Q_{LW} + Q_{SW}) \simeq 200$ W m^{-2}. There is a large correspondence between large and positive Q_s in spring and summer (Figure 5d), shallow mixed layer, and negligible percentage of the uML to overturning instabilities (Figures 7d and 7e). Although the *trade* winds in summer and spring are weaker than winter Northerly winds, in conjunction with the large rates of evaporation in the GoM (Yu et al., 2007), they can notably reduce the total equivalent heat fluxes (even reversing the sign of radiative fluxes; see yellow shading in Figure 5d), leading to a mixed layer unstable to GIs all year round (Figures 4b, 4d and 4e).

The GIs are by far the most frequent and largely distributed within the SBL (Figures 4b and 4d). The Probability Density Function (PDF) of ϕ_{Ri_b} indicates that this mode of instability is adjusting toward angles of $-135°$ and that extracts most of the potential energy from heat loss (Figures 10a and C1). The seasonal cycle reported here, however, is not observed at the periphery of the LCE pointing out that different processes are at work across the LCE. Symmetrical instability is more likely to occur at the periphery of the LCE (Figures 4c, 4d and 7a) driven by the extraction of mixed-layer PV by negative EBF (Figures 6 and 7d) rather than the preconditioning reduction of mixed-layer PV driven by heat loss. Although, the SIs apparently do not show a seasonal preference, they are most frequent when lateral buoyancy gradients are large (i.e., filaments/fronts) and the increase of surface forcing during autumn and winter. Moreover, conditions for the occurrence of ISIs are almost never attained (<10%) across the LCE, although we observed one case of expected development of ISIs during the largest down-front wind event of the year of measurements.

The radial composites across the LCE reveal some key findings regarding cross-eddy structure (Figure 7). GSIs/GIs are largely expected inside the LCE (30% of the MLD; Figure 7a), in particular during winter (80% of the MLD; Figure 4b). At the periphery of the LCE, enhanced Ekman equivalent heat flux (Figure 7d) associated

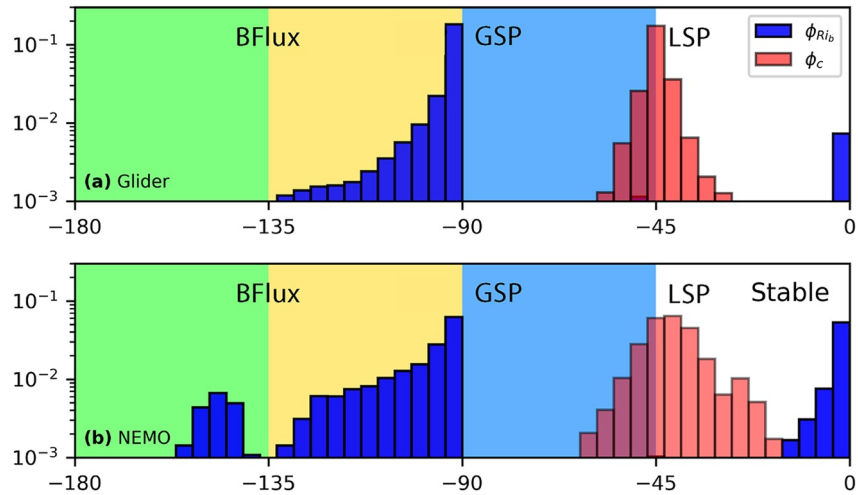

Figure 10. Probability Density Function (PDF) of ϕ_{Ri_b} and ϕ_c using (a) all the glider observations (Figure 4d) and (b) the section AB of the numerical LCE (Figures 9b and 9e). Acronym BFlux refers to the gain of kinetic energy from buoyancy flux and GSP (geostrophic shear production) and LSP (lateral shear production) from the geostrophic flow.

with large horizontal buoyancy gradients (Figure 7b) increases the occurrence of SIs, about 35% of the MLD (Figure 7a); been higher than the %uML to GSIs/GIs at the LCE's periphery.

Two down-front wind events in December 2016 were studied in detail (Figures 8a–8e), with significant differences between the two: the depth of the mixed layer of 40 m versus 160 m, the intensity of the Ekman buoyancy heat fluxes of −10,351 W m^{-2} versus −83 W m^{-2}, and the intensity of horizontal buoyancy gradients evidenced by the vertical distribution of the density shown in Figure 8d (compare stacked vertical isopycnals on 8–10 vs. 19–22 December). The results suggest that under conditions of strong negative turbulent heat fluxes and Ekman heat fluxes, shallower mixed layers with large horizontal buoyancy gradients (first event) promote the occurrence of SIs while deeper mixed layers with weaker buoyancy gradients (second event) lead to GSIs/GIs. It should be noted that $Q_{Ek} + Q_s$ is 20 times larger during the first wind event than the second, which favors the occurrence of ISIs during the first case.

We show observational evidences, using high-resolution gliders observations, of GSIs and SIs/ISIs within and at the periphery of the LCE, respectively. Joyce et al. (2009), Thomas and Joyce (2010), and Thomas et al. (2013), using hydrographical, biogeochemical, and Acoustic Doppler Current Profiler (ADCP) surveys, show the occurrence of SIs, subduction, and winter subtropical mode water formation at the flanks of the Gulf Stream with EBFs and cross-front mesoscale buoyancy gradients similar to this work. At the beginning of December 2016, a cyclonic meander is strained between the coast and the LCE, forming a cold filament elongating northwards (Figures 1c, 2a, and 8b). It may be considered that during the extreme down-front wind event that occurred on 9 December across the cyclonic filament, enhanced mixing through ISIs efficiently homogenizes the thermohaline properties and brings the mixed-layer PV back to zero. E. D'Asaro et al. (2011) using a combination of Lagrangian measurements (hull-mounted temperature, floats, and Triaxus) were able to directly measure enhanced rates of energy dissipation at the cyclonic flank of the Kuroshio driven by SIs. Quasi geostrophic theory at a front (Hoskins, 1982; Spall, 1995) and TTW across a submesoscale cyclonic cold filament (Gula et al., 2014; McWilliams, 2016) predicts downwelling of fluid parcels within the cold filament (center) and upwelling on both light sides (outer flanks). This ageostrophic secondary circulation, subducts recently created low-PV fluid parcels of the mixed layer into the thermocline (Figure 8c) that could contribute to mode water formation. Subduction of surface waters across the periphery of an anticyclonic eddy has also been reported in Tasman Sea using high-resolution glider sections of dissolved oxygen and numerical modeling (Brannigan et al., 2017). Similarly, in Tasman Sea (Archer et al., 2020), using high-resolution hydrographic and velocity measurements across a mesoscale dipole axis shows that subducted low-PV waters quickly develop anticyclonic circulation yielding submesoscale intrathermocline eddies.

The numerical simulations reproduce adequately the main processes that prompt the destabilization of the mixed layer through frictional and diabatic extraction of PV. The magnitude of simulated buoyancy gradients across the fronts/filaments ($\partial b/\partial x$) and the PV is slightly larger than the observations due to the coarser horizontal resolution of the glider observations (~2.7 km; Figure 1a) versus high-resolution numerical simulations (1 km) as well as the angle between the glider trajectory and the orientation of the fronts/filaments. Note, however, our sampling strategy attempts to reduce this underestimation by crossing the periphery of the eddies along their maximum ADT gradients. The magnitude of Ekman equivalent heat flux is a function of the relative orientation between geostrophic vertical shear and wind stress, and their magnitudes. The extreme Q_{Ek} in the numerical simulations are slightly weaker to those observed during extreme wind events (i.e., Northerly winds). Since $\partial b/\partial x$ in the simulations are of similar magnitude than the glider-observed $\partial b/\partial x$, these results suggest that Q_{Ek} computed using the along-track glider data is slightly overestimated because the actual geostrophic vertical shear and wind stress vectors were not exactly parallel (Figure 15c in Thompson et al. [2016]). Nevertheless, the values of Q_{Ek} reported in this work are in agreement with the values computed using glider data in the North Atlantic gyre (Thompson et al., 2016), in the Circumpolar Current (Viglione et al., 2018) and recently in the Mediterranean Sea (Bosse et al., 2021) with values of $O(|Q_{Ek}|) \simeq 1{,}000$ W m^2 for $O(\partial b/\partial x) \simeq 1 \times 10^{-7}$ s^{-2} (Figures 6, 7b and 7d). Similar extreme Q_{Ek} of 12,000 W m^{-2} is found at the Gulf Stream (Thomas et al., 2013).

The numerical diagnostics of overturning instabilities (Figures 9c–9e) are in striking agreement with the observations (Figures 3, 4d and 6). The dominant mode of instability within the modeled LCE is also the mixed GSIs. Additionally, the PDF of ϕ_{Ri_b} (Figure 10b) has a skewness toward angles of −90°. GIs diagnosed from instability angle $\left(\phi_{Ri_b} < -135°\right)$ in the uppermost mixed layer are solved by the numerical model (Figure 10b) but filtered out in the glider data (Figure 10a). GIs diagnosed as regions of $N^2 < -2 \times 10^{-5}$ s^{-2} are however solved and they are driven the whole year by significant latent heat fluxes although the most favorable conditions are reached during autumn and, especially, winter. Using linear rather than optimal interpolation increases the number of realizations of instability angles for SIs and ISIs at the periphery and inside the LCE because the along-track buoyancy gradients are enhanced elsewhere.

The cross-eddy composite structure of overturning instabilities shown in Figure 7a suggests a mixed layer unstable to GSIs/GIs inside the eddy and to SIs at the periphery of the LCE forced by down-front winds, similar to the results reported in a numerical anticyclonic mesoscale eddy (Zhong et al., 2017). Furthermore, using CTD and ADCP data across an anticyclonic eddy in South China Sea conducted in winter, the authors suggest that the whole eddy is potentially unstable to SIs with $\phi_{Ri_b} \simeq -90°$ nearly everywhere which agrees very well with the PDF of ϕ_{Ri_b} across the LCE (Figure 10a). It should be noticed that the authors do not fully test for SIs since they do not inform whether the instability is active or not, based on the ratio between the convective and SBL (Taylor & Ferrari, 2010). Indeed, similar to this work, instability angle ϕ_{Ri_b} being about −90° inside the anticyclonic eddy might be attributed to winter gravitational convection rather than forced SI.

The glider sampled Poseidon along SW-NE sections (Figure 1) crossing consistently fresh submesoscale filaments wrapping around the eddy periphery (Figure 2b). These filaments are negative anomalies of density with large lateral buoyancy gradients enhanced on the inner flank (anticyclonic side) of the fresh water filament. The vertical shear (and horizontal buoyancy gradients) increases significantly (Figure 2d) favoring the occurrence of overturning instabilities. An example, on 14–16 December, the fresh water filament of about 30 km horizontal scale is clearly evidenced by a concave low-density anomaly reaching the base of the shallow mixed layer (Figure 8). In this case, and because the atmospheric forcing was weak (Figure 5b), BCIs are expected to dominate at the density front. Even though the total heat fluxes are positive, negative EBF decreases the PV at the westward flank of the fresh water filament and could promote the occurrence of SIs. The restratifying effect is clearer on the eastward flank of the filament (inner side of the LCE) where the isopycnals of the filament are tilted related to the westwards flank where they are almost vertical, and the temperature and the optical backscatter are notably reduced along the glider track suggesting lateral buoyancy exchange between the filament and the eddy interior. Coastal, riverine waters are common in the surface layer of the GoM (Weatherly et al., 2003). The glider sampled at least five more fresh water filaments during the whole year of measurements. Two of them, on 14 February and 25 March 2017, we observe the occurrence of GSIs at the inner flank of the filament associated with large $Q_{Ek} < 0$ there (not shown). Once the negative PV is restored in the mixed layer ($Ri_b \simeq 1$), BCIs can arise at these filaments, generating baroclinic submesoscale eddies, that provide intense lateral buoyancy fluxes (Haine & Marshall, 1998).

Overturning instabilities at the peripheries exist and may have important implications on the transformation of water masses of the LCE by redistributing laterally and vertically buoyancy within the mixed layer. Although, we do not directly measured rates of energy dissipation during the glider measurements and did not have available vertical profiles of ADCP to diagnose shear-derived parameterizations of mixing, the overturning instabilities discussed in this paper shed some light on the processes that could explain the intense loss of heat content in the LCEs during the first months of their lives shown in Meunier et al. (2020). Studying the dynamics of these submesoscale processes is thus important to understand the thermohaline balance in the mixed layer of the GoM, including the LC-system, which may have implications on the heat and salt transport by the Gulf Stream toward higher latitudes and climate change.

8. Concluding Remarks

The LCE Poseidon was surveyed intensively during August 2016 and August 2017 providing uninterrupted high-resolution density data during the whole seasonal cycle in the GoM. A overturning instability analysis is used to identify regions across each cross-frontal section of the LCE Poseidon susceptible to gravitational, gravitational-symmetric, and symmetric and inertia-symmetric instabilities. The most important findings of this study can be summarized as follows:

1. Even though the seasonal convection is dominant in the warm core eddies, this does not hold at the periphery of the eddy and lateral buoyancy gradients lead to a radial transition between the GIs and SIs in the eddy.
2. Filamentogenesis between the LCE Poseidon and surrounding mesoscale cyclones increases the EBF, TTW, and baroclinic heat fluxes by increasing lateral buoyancy gradients.
3. LCE's radial distribution of overturning instabilities: the percentage of unstable mixed layer to GIs is enhanced inside the LCE while favorable conditions to SIs are likely to occur at the LCE's periphery.
4. Stratification at the LCE's periphery and thermocline significantly suppresses the occurrence of GIs.
5. The case study provides observational evidence of unstable mixed layer to symmetric and ISI across a cold filament by the destabilizing EBF driven by down-front winds.
6. Numerical diagnostics are in very good agreement with observations: favorable conditions for (a) GSIs filling the entire mixed layer in the eddy's core and (b) SIs driven by down-front winds over submesoscale filaments, mostly at the periphery of the eddy.

The seasonality of GIs inside the LCE Poseidon reported in this work is in agreement with the increased erosion of the subsurface salinity maximum of the LCE's core in winter reported by Sosa-Gutiérrez et al. (2020). The favorable conditions to SIs at the LCE's periphery shed some light on the submesoscale physical processes responsible for the lateral dispersion of heat and salt content of LCEs as they propagate westwards (Meunier et al., 2020).

Appendix A: Nondimensional Scaling Ratios of Vertical PV Fluxes

The extraction of Ertel PV

$$q = (f\mathbf{k} + \nabla \times \mathbf{u}) \cdot \nabla b \tag{A1}$$

in the mixed layer is driven by diabatic and frictional processes. The local rate of change of the PV

$$\frac{\partial q}{\partial t} = -\nabla \cdot \mathbf{J}, \tag{A2}$$

is a function of the divergence of the PV flux ($\mathbf{J}$)

$$\mathbf{J} = \underbrace{\mathbf{u}q}_{advective\,(J_A)} + \underbrace{\nabla b \times \mathbf{F}}_{frictional\,(J_F)} - \underbrace{(f\mathbf{k} + \nabla \times \mathbf{u})D}_{diabatic\,(J_D)}, \tag{A3}$$

where $\mathbf{u}$ is the velocity, $\mathbf{F} = \partial/\partial z\,(\nu_E \partial \mathbf{u}/\partial z)$ is the frictional force (ν_E eddy viscosity), and $D = db/dt$ is the material rate of change of buoyancy. Because of the impermeability theorems (Haynes & McIntyre, 1987), the reduction of the PV of a volume control constrained between two isopycnal surfaces occurs only if the surface

PV flux is upward (vertical fluxes from the ocean to atmosphere are positive, which is the convention followed in Thomas (2005); Thomas, 2005; Wenegrat & Thomas, 2018). Two main mechanisms drive vertical PV fluxes: (a) diabatic surface buoyancy fluxes and (b) wind-induced (frictional) PV fluxes. Surface cooling ($D < 0$) drives GIs that reduce the stratification which is traditionally related to destruction of PV (upward diabatic flux; $J_D^z > 0$). The vertical component of the wind-induced (frictional) PV fluxes is a function of the relative orientation between the geostrophic vertical shear and frictional forces

$$J_F^z = f \frac{\partial \mathbf{u}_h^g}{\partial z} \cdot \mathbf{F}, \tag{A4}$$

where $\partial \mathbf{u}_h^g / \partial z$ is related to $\nabla_h b$ through the thermal-wind balance

$$-f \mathbf{k} \times \partial \mathbf{u}_h^g / \partial z = \nabla_h b. \tag{A5}$$

The frictional forces are typically oriented in the direction of the wind stress ($\boldsymbol{\tau}_h$). Hence, J_F^z is upward (downward) when the wind stress blows in the direction (in the opposite direction) of the frontal geostrophic current, that is, down-front (up-front) winds. Assuming that J_F^z is vertically uniform, the vertically integrated J_F^z between the surface and the convective layer depth (h_c) can be written as (Wenegrat & Thomas, 2018)

$$J_F^z \simeq \frac{f}{h_c} [\underbrace{\mathbf{M}_e \cdot \nabla_h b}_{EBF} + \underbrace{\mathbf{M}_{TTW} \cdot \nabla_h b}_{EBF_g}], \tag{A6}$$

where $\mathbf{M}_e = (1/\rho_o f) \mathbf{k} \times \tau_h$ is the linear Ekman transport and $\mathbf{M}_{TTW} = (1/\rho_o f)\, \mathbf{k} \times \boldsymbol{\tau}_h^g \approx \left(\nu_E / f^2\right) \nabla_h b$ is the "TTW transport" associated with geostrophic stress $\boldsymbol{\tau}_h^g = -\rho_o \nu_E \partial \mathbf{u}_h^g / \partial z$ at $z = 0$ (Bachman & Taylor, 2016). It should be clarified that the sign convention used for destratifying EBF in Section 3.3 (negative) is opposite than the one used in this appendix. EBF (EBF_g) is related to the advection of buoyancy by the vertically integrated Ekman flow (by the TTW flow in the Ekman layer). The former injects (destroy) PV at the sea surface associated with up-front (down-front) winds while the latter always implies injection of PV in the mixed layer from the thermocline (McWilliams, 2016; Wenegrat & Thomas, 2018).

Following Wenegrat and Thomas (2018), the relative importance between $\boldsymbol{J}^{TTW}$ and $\boldsymbol{J}^{WIND}$ can be scaled using the ratio

$$\gamma_F = \frac{J_F^{TTW} + J_D^{TTW}}{J_F^{WIND} + J_D^{WIND}} = \frac{(f/h) EBF_g}{(f/h) EBF} = \frac{\mathbf{M}_{TTW} \cdot \nabla_h b}{\mathbf{M}_e \cdot \nabla_h b}, \tag{A7}$$

where J_D^{TTW} and J_D^{WIND} are diabatic PV fluxes due to vertical shear and surface wind stress, and h is the depth of the SBL; therefore, it can be scaled to

$$\gamma_F \approx \frac{\nu_E \sigma_{\theta_0} |\nabla_h b|}{f |\boldsymbol{\tau}_h|}, \tag{A8}$$

where ν_E is the eddy viscosity. Comparison between the vertical PV fluxes due to TTW flow with vertical PV fluxes due to atmospheric buoyancy flux (B_0) gives the ratio

$$\gamma_q = \frac{J_F^{TTW} + J_D^{TTW}}{\boldsymbol{J}^{BUOY}} = \frac{(f/h) EBF_g}{(f/h) B_0} \approx \frac{\nu_E |\nabla_h b|^2}{|f^2 B_0|}, \tag{A9}$$

and the relative importance of frictional versus diabatic processes can be diagnosed using the ratio

$$\gamma_w = \gamma_q / \gamma_F = \frac{J_F^{WIND} + J_D^{WIND}}{\boldsymbol{J}^{BUOY}} = \frac{(f/h) EBF}{(f/h) B_0} \approx \frac{|\boldsymbol{\tau}_h| |\nabla_h b|}{\sigma_{\theta_0} |f B_0|}. \tag{A10}$$

Hence, neglecting the vertical component of the advective PV flux in Equation A3, the total vertical PV flux (J^z) in a volume integrated between two isopycnals is only due to diabatic and frictional processes

$$J^z = J_D^z + J_F^z = \frac{f}{h} \left[EBF + EBF_g + B_0 \right]. \tag{A11}$$

A parameterization of the buoyancy flux due to BCIs is $BF_{FK08} = C_q H^2 |\nabla_h b|^2 / f$ which allows for definition of a ratio that compares the relative strength between the PV fluxes due to TTW flow and the vertical PV fluxes arising from BCIs

$$\gamma_{BCI} = \frac{J_F^{TTW} + J_D^{TTW}}{J^{BCI}} = \frac{(f/h)EBF_g}{(f/h)BF_{FK08}} \approx \frac{\nu_E}{f C_q H^2}, \tag{A12}$$

where H represents the depth of the SBL. This ratio, however, needs to be interpreted with caution because of the large range of variability associated with efficiency coefficient C_q which can vary from 0.06 to 1 (Figure A1a). This is because this ratio will not be computed.

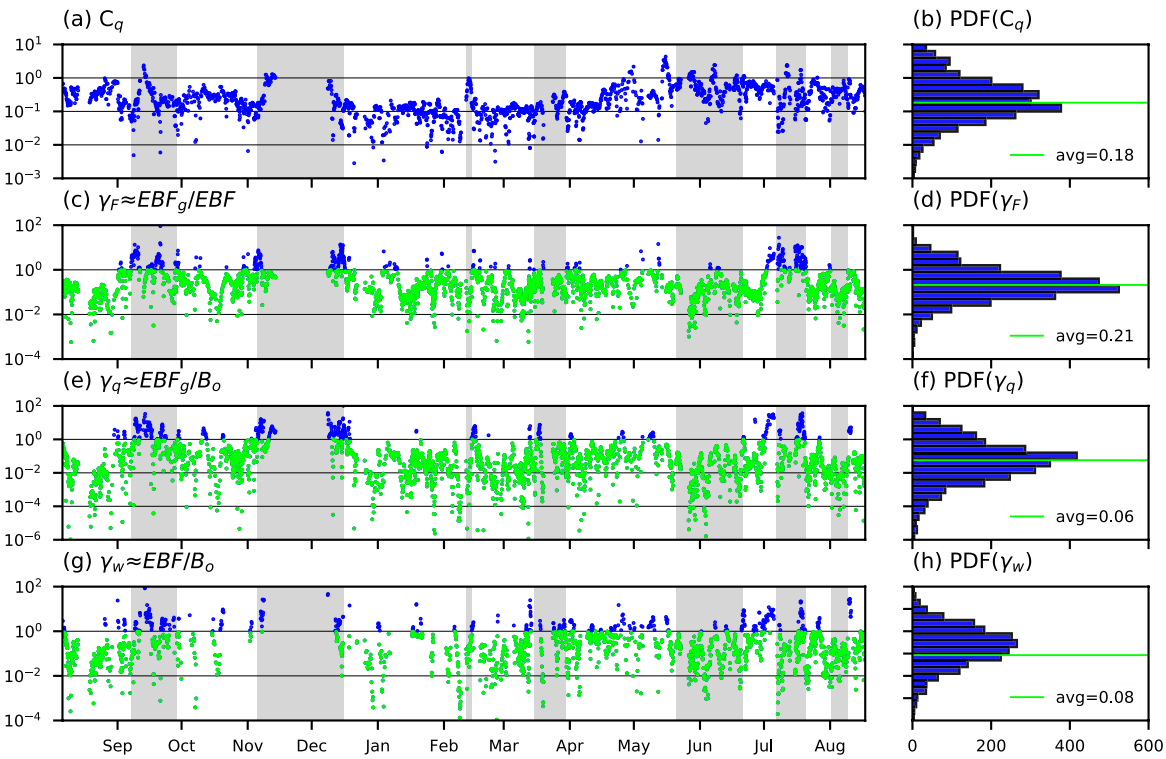

Figure A1. Atmospheric forcing ratios and their PDFs: (a, b) $C_q = \frac{0.1u^*}{fH}$, (c, d) γ_F, (e, f) γ_q, and (g, h) γ_w. Blue (light green) dots in panels (b)–(d) indicate ratios above unity.

Figure A1 shows the time evolution of the relevant ratios between the scaling for the vertical PV fluxes. Typically, diabatic reduction of PV is persistent all year round and at any location; frictional (Ekman and TTW) buoyancy fluxes are dominant at the periphery of the LCE Poseidon.

Appendix B: Mixed-Layer Instability Conditions

In presence of geostrophic vertical shear, SIs or slantwise convections arise when PV takes the opposite sign of f (Hoskins, 1982):

$$fq = -|\nabla_h b|^2 + f(\zeta + f)N^2 = fN^2\left(\zeta/f + 1 - \frac{1}{Ri_b}\right) < 0. \tag{B1}$$

Oppositely, centrifugal instabilities (CIs) extract the energy from geostrophic lateral shear and arise when $Ro < -1$ which guarantees negative PV. GIs convert convective available potential energy to kinetic energy and arise when (Haine & Marshall, 1998)

$$N^2 < 0. \tag{B2}$$

From Equation B1, the mixed layer is unstable to overturning instabilities when

$$f N^2 \left(Ro + 1 - \frac{1}{Ri_b} \right) < 0, \tag{B3}$$

which strongly relies on the sign of N^2 and Ro. Depending on the sign N^2, three possible instability conditions can be delineated:

1. Unstable to SIs: $N^2 > 0$ and $f > 0$ (northern hemisphere)

$$Ro + 1 < \frac{1}{Ri_b} \text{ and} \tag{B4}$$

2. Unstable to ISIs: $N^2 < 0, f > 0$, and $\zeta^g < 0$ and

$$Ro + 1 < \frac{1}{Ri_b} < 1 \tag{B5}$$

3. Unstable to mixed GIs and SIs (i.e., GSIs): $N^2 < 0$ and $f > 0$

$$Ro + 1 > \frac{1}{Ri_b} \tag{B6}$$

Finally, for flows with large $Ri_b \geq 1$ (for which SIs die), baroclinic instabilities (BCIs) can develop (Boccaletti et al., 2007; Fox-Kemper et al., 2008; Haine & Marshall, 1998). BCIs in the mixed layer are feed by the potential energy of slopping isopycnals (i.e., fronts/filaments) and they drive positive values of vertical buoyancy flux, restratifying the mixed layer through the injection of high-PV filaments from the thermocline along the buoyancy surfaces.

Appendix C: Temperature–Salinity (T–S) Diagram

The temperature–salinity (T–S) diagram shows the LCE water properties and water mass transformation during a full seasonal cycle (Figure C1). The upper 200 m of the young LCE Poseidon (summer and autumn 2016) is mainly formed by water masses of Caribbean origin in the upper ocean (Figure C1; blue dots): Caribbean Surface Water (CSW; 50–150 m) and NASUW (150–230 m). Submesoscale filaments are identified in the T–S diagram as bands of low salinity and nearly homogeneous temperature that can occur any season of the year. The Warm Core Rings detached from the Loop Current decay as they propagate westwards (Lipphardt et al., 2008; Meunier et al., 2020) mixing the NASUW with fresher surrounding waters (Figure C1; yellow dots), forming GCW and Caribbean Surface Water remnant (CSWr). The old LCE Poseidon (summer 2017) no longer has the signal of the NASUW (Figure C1; green dots). The T–S diagram clearly depicts the transformation of NASUW to GCW within the LCE Poseidon during winter as reported in detail in Sosa-Gutiérrez et al. (2020).

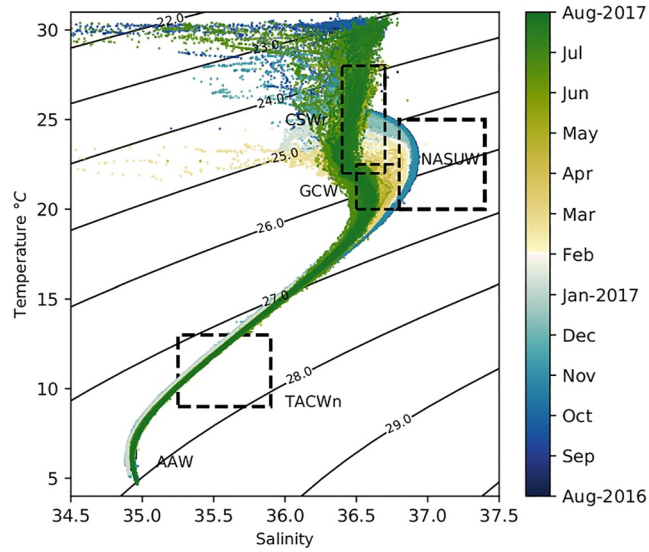

Figure C1. Temperature (°C)–salinity (*T*–*S*) diagram for the whole year of thermohaline measurements, color coded with time. The different water masses ubiquitous in the upper 1,000 m depth of the LCE Poseidon are: Caribbean Surface Water remnant (CSWr; located between 50 and 150 m), North Atlantic Subtropical UnderWater (NASUW; located between 150 and 230 m), Gulf Common Water (GCW; 50–150 m), Tropical Atlantic Central Water (TACW; located between 300 and 700 m), and the Antarctic Intermediate Water (AAIW; located between 740 and 900 m). Depth ranges are extracted from Portela et al. (2018).

Data Availability Statement

The altimeter data were produced by Ssalto/Duacs and distributed by Aviso, with support from CNES (http://www.aviso.altimetry.fr/duacs/), satellite sea surface temperature is downloaded from NASA's Physical Oceanography Distributed Active Archive Center (PODAAC; https://podaac-www.jpl.nasa.gov/), gridded surface winds and air-sea heat fluxes are produced by IFREMER and distributed by Copernicus Marine Environment Monitoring System (CMEMS; http://marine.copernicus.eu) and IFREMER (https://wwz.ifremer.fr/oceanheatflux/Data), respectively, MODIS ocean color is distributed by the Ocean Biology Distributed Active Archive Center (OBDAAC; https://oceancolor.gsfc.nasa.gov/), ERA5 downward and upward radiative fluxes at surface are obtained from Copernicus, and standard meteorological data were obtained from the National Data Buoy Center (NDBC; https://www.ndbc.noaa.gov/). The raw glider data can be visualized on the GMOG's webpage (https://gliders.cicese.mx/).

Acknowledgments
This research is funded by the National Council of Science and Technology of Mexico-Mexican Ministry of Energy-Hydrocarbon Trust, project 201441. This is a contribution of the Gulf of Mexico Research Consortium (CIGoM). Thanks are due to the Group of Monitoring the Ocean with Gliders (GMOG), specially the field team that has been involved in collecting hydrographic measurements during the four glider missions. We acknowledge to public oceanographic and meteorological data providers. J. C. is grateful to Pr. Paula Brunius, Pr. Julio Sheinbaum, and Pr. Reginaldo Durazo, members of his PhD committee. We acknowledge three anonymous reviewers for their fruitful comments and suggestions that have notably improved the paper.

References

Archer, M., Schaeffer, A., Keating, S., Roughan, M., Holmes, R., & Siegelman, L. (2020). Observations of submesoscale variability and frontal subduction within the mesoscale eddy field of the Tasman Sea. *Journal of Physical Oceanography*, *50*(5), 1509–1529. https://doi.org/10.1175/JPO-D-19-0131.1

Bachman, S. D., & Taylor, J. R. (2016). Numerical simulations of the equilibrium between eddy-induced restratification and vertical mixing. *Journal of Physical Oceanography*, *46*(3), 919–935. https://doi.org/10.1175/JPO-D-15-0110.1

Barkan, R., Molemaker, M. J., Srinivasan, K., McWilliams, J. C., & D'Asaro, E. A. (2019). The role of horizontal divergence in submesoscale frontogenesis. *Journal of Physical Oceanography*, *49*(6), 1593–1618. https://doi.org/10.1175/JPO-D-18-0162.1

Barnes, S. L. (1994). Applications of the Barnes objective analysis scheme. Part III: Tuning for minimum error. *Journal of Atmospheric and Oceanic Technology*, *11*(6), 1459–1479. https://doi.org/10.1175/1520-0426(1994)011<1459:AOTBOA>2.0.CO;2

Behrenfeld, M. J., & Boss, E. (2006). Beam attenuation and chlorophyll concentration as alternative optical indices of phytoplankton biomass. *Journal of Marine Research*, *64*(3), 431–451.

Belmonte Rivas, M., & Stoffelen, A. (2019). Characterizing era-interim and era5 surface wind biases using ascat. *Ocean Science*, *15*(3), 831–852. https://doi.org/10.5194/os-15-831-2019,2019

Bentamy, A., Grodsky, S. A., Katsaros, K., Mestas-Nuñez, A. M., Blanke, B., & Desbiolles, F. (2013). Improvement in air–sea flux estimates derived from satellite observations. *International Journal of Remote Sensing*, *34*(14), 5243–5261. https://doi.org/10.1080/01431161.2013.787502

Boccaletti, G., Ferrari, R., & Fox-Kemper, B. (2007). Mixed layer instabilities and restratification. *Journal of Physical Oceanography*, *37*(9), 2228–2250. https://doi.org/10.1175/JPO3101.1

Bosse, A., Testor, P., Damien, P., Estournel, C., Marsaleix, P., Mortier, L., et al. (2021). Wind-forced submesoscale symmetric instability around deep convection in the northwestern Mediterranean Sea. *Fluids*, *6*(3), 123. https://doi.org/10.3390/fluids6030123

Brannigan, L. (2016). Intense submesoscale upwelling in anticyclonic eddies. *Geophysical Research Letters*, *43*, 3360–3369. https://doi.org/10.1002/2016GL067926

Brannigan, L., Marshall, D. P., Naveira Garabato, A. C., Nurser, A. G., & Kaiser, J. (2017). Submesoscale instabilities in mesoscale eddies. *Journal of Physical Oceanography*, *47*(12), 3061–3085. https://doi.org/10.1175/JPO-D-16-0178.1

Buckingham, C. E., Naveira Garabato, A. C., Thompson, A. F., Brannigan, L., Lazar, A., Marshall, D. P., et al. (2016). Seasonality of submesoscale flows in the ocean surface boundary layer. *Geophysical Research Letters*, *43*, 2118–2126. https://doi.org/10.1002/2016GL068009

Callies, J., Ferrari, R., Klymak, J. M., & Gula, J. (2015). Seasonality in submesoscale turbulence. *Nature Communications*, *6*(1), 1–8. https://doi.org/10.1038/ncomms7862

Capet, X., McWilliams, J. C., Molemaker, M. J., & Shchepetkin, A. (2008b). Mesoscale to submesoscale transition in the California current system. Part II: Frontal processes. *Journal of Physical Oceanography*, *38*(1), 44–64. https://doi.org/10.1175/2007JPO3672.1

Capet, X., McWilliams, J. C., Molemaker, M. J., & Shchepetkin, A. F. (2008a). Mesoscale to submesoscale transition in the California current system. Part I: Flow structure, eddy flux, and observational tests. *Journal of Physical Oceanography*, *38*(1), 29–43. https://doi.org/10.1175/2007JPO3671.1

Capet, X., McWilliams, J. C., Molemaker, M. J., & Shchepetkin, A. F. (2008c). Mesoscale to submesoscale transition in the California current system. Part III: Energy balance and flux. *Journal of Physical Oceanography*, *38*(10), 2256–2269. https://doi.org/10.1175/2008JPO3810.1

Chaigneau, A., Gizolme, A., & Grados, C. (2008). Mesoscale eddies off Peru in altimeter records: Identification algorithms and eddy spatio-temporal patterns. *Progress in Oceanography*, *79*(2–4), 106–119. https://doi.org/10.1016/j.pocean.2008.10.013

D'Asaro, E., Lee, C., Rainville, L., Harcourt, R., & Thomas, L. (2011). Enhanced turbulence and energy dissipation at ocean fronts. *Science*, *332*(6027), 318–322. https://doi.org/10.1126/science.1201515

D'Asaro, E. A., Shcherbina, A. Y., Klymak, J. M., Molemaker, J., Novelli, G., Guigand, C. M., et al. (2018). Ocean convergence and the dispersion of flotsam. *Proceedings of the National Academy of Sciences of the United States of America*, *115*(6), 1162–1167. https://doi.org/10.1073/pnas.1718453115

Decharme, B., Delire, C., Minvielle, M., Colin, J., Vergnes, J.-P., Alias, A., et al. (2019). Recent changes in the ISBA-CTRIP land surface system for use in the CNRM-CM6 climate model and in global off-line hydrological applications. *Journal of Advances in Modeling Earth Systems*, *11*, 1207–1252. https://doi.org/10.1029/2018MS001545

Dussin, R., Barnier, B., & Brodeau, L. (2014). Atmospheric forcing data sets to drive eddy-resolving global ocean general circulation models. In *EGU General Assembly conference abstracts* (p. 1716).

Edson, J. B., Jampana, V., Weller, R. A., Bigorre, S. P., Plueddemann, A. J., Fairall, C. W., et al. (2013). On the exchange of momentum over the open ocean. *Journal of Physical Oceanography*, *43*(8), 1589–1610. https://doi.org/10.1175/JPO-D-12-0173.1

Fox-Kemper, B., Ferrari, R., & Hallberg, R. (2008). Parameterization of mixed layer eddies. Part I: Theory and diagnosis. *Journal of Physical Oceanography*, *38*(6), 1145–1165. https://doi.org/10.1175/2007JPO3792.1

Gaube, P., McGillicuddy, D. J., Jr., Chelton, D. B., Behrenfeld, M. J., & Strutton, P. G. (2014). Regional variations in the influence of mesoscale eddies on near-surface chlorophyll. *Journal of Geophysical Research: Oceans*, *119*, 8195–8220. https://doi.org/10.1002/2014JC010111

Gula, J., Blacic, T. M., & Todd, R. E. (2019). Submesoscale coherent vortices in the Gulf Stream. *Geophysical Research Letters*, *46*, 2704–2714. https://doi.org/10.1029/2019GL081919

Gula, J., Molemaker, M., & McWilliams, J. (2015). Topographic vorticity generation, submesoscale instability and vortex street formation in the Gulf Stream. *Geophysical Research Letters*, *42*, 4054–4062. https://doi.org/10.1002/2015GL063731

Gula, J., Molemaker, M. J., & McWilliams, J. C. (2014). Submesoscale cold filaments in the Gulf Stream. *Journal of Physical Oceanography*, *44*(10), 2617–2643. https://doi.org/10.1175/JPO-D-14-0029.1

Haine, T. W., & Marshall, J. (1998). Gravitational, symmetric, and baroclinic instability of the ocean mixed layer. *Journal of Physical Oceanography*, *28*(4), 634–658. https://doi.org/10.1175/1520-0485(1998)028<0634:GSABIO>2.0.CO;2

Haynes, P. H., & McIntyre, M. E. (1987). On the evolution of vorticity and potential vorticity in the presence of diabatic heating and frictional or other forces. *Journal of Atmospheric Sciences*, *44*(5), 828–841.

Hersbach, H., Bell, B., Berrisford, P., Hirahara, S., Horányi, A., Muñoz-Sabater, J., et al. (2020). The ERA5 global reanalysis. *Quarterly Journal of the Royal Meteorological Society*, *146*(730), 1999–2049. https://doi.org/10.1002/qj.3803

Hoskins, B. J. (1982). The mathematical theory of frontogenesis. *Annual Review of Fluid Mechanics*, *14*(1), 131–151. https://doi.org/10.1146/annurev.fl.14.010182.001023

Joyce, T. M., Thomas, L., & Bahr, F. (2009). Wintertime observations of subtropical mode water formation within the Gulf Stream. *Geophysical Research Letters*, *36*, L02607. https://doi.org/10.1029/2008GL035918

Kara, A. B., Rochford, P. A., & Hurlburt, H. E. (2000). An optimal definition for ocean mixed layer depth. *Journal of Geophysical Research*, *105*(C7), 16803–16821. https://doi.org/10.1029/2000JC900072

Lapeyre, G., Klein, P., & Hua, B. L. (2006). Oceanic restratification forced by surface frontogenesis. *Journal of Physical Oceanography*, *36*(8), 1577–1590. https://doi.org/10.1175/JPO2923.1

Lipphardt, B., Poje, A., Kirwan, A., Kantha, L., & Zweng, M. (2008). Death of three loop current rings. *Journal of Marine Research*, *66*(1), 25–60.

Luna-Niño, R., & Cavazos, T. (2018). Formation of a coastal barrier jet in the Gulf of Mexico due to the interaction of cold fronts with the sierra Madre Oriental mountain range. *Quarterly Journal of the Royal Meteorological Society*, *144*(710), 115–128. https://doi.org/10.1002/qj.3188

Madec, G. (2016). The NEMO team: NEMO ocean engine. *Note du Pôle de modélisation, Institut Pierre-Simon Laplace (IPSL), France*, *27*, 1288–1619.

Mahadevan, A. (2016). The impact of submesoscale physics on primary productivity of plankton. *Annual Review of Marine Science*, *8*, 161–184. https://doi.org/10.1146/annurev-marine-010814-015912

Mahadevan, A., & Tandon, A. (2006). An analysis of mechanisms for submesoscale vertical motion at ocean fronts. *Ocean Modelling*, *14*(3–4), 241–256. https://doi.org/10.1016/j.ocemod.2006.05.006

Mahadevan, A., Tandon, A., & Ferrari, R. (2010). Rapid changes in mixed layer stratification driven by submesoscale instabilities and winds. *Journal of Geophysical Research*, *115*, C03017. https://doi.org/10.1029/2008JC005203

Marshall, J. C., & Nurser, A. G. (1992). Fluid dynamics of oceanic thermocline ventilation. *Journal of Physical Oceanography*, *22*(6), 583–595. https://doi.org/10.1175/1520-0485(1992)022<0583:FDOOTV>2.0.CO;2

McWilliams, J. C. (2016). Submesoscale currents in the ocean. *Proceedings of the Royal Society A: Mathematical, Physical & Engineering Sciences*, *472*(2189), 20160117. https://doi.org/10.1098/rspa.2016.0117

McWilliams, J. C. (2017). Submesoscale surface fronts and filaments: Secondary circulation, buoyancy flux, and frontogenesis. *Journal of Fluid Mechanics*, *823*, 391–432. https://doi.org/10.1017/jfm.2017.294

Meunier, T., Pallàs-Sanz, E., Tenreiro, M., Portela, E., Ochoa, J., Ruiz-Angulo, A., & Cusí, S. (2018). The vertical structure of a Loop Current Eddy. *Journal of Geophysical Research: Oceans*, *123*, 6070–6090. https://doi.org/10.1029/2018JC013801

Meunier, T., Sheinbaum, J., Pallàs-Sanz, E., Tenreiro, M., Ochoa, J., Ruiz-Angulo, A., et al. (2020). Heat content anomaly and decay of warm-core rings: The case of the Gulf of Mexico. *Geophysical Research Letters*, *47*, e2019GL085600. https://doi.org/10.1029/2019GL085600

Meunier, T., Tenreiro, M., Pallàs-Sanz, E., Ochoa, J., Ruiz-Angulo, A., Portela, E., et al. (2018). Intrathermocline eddies embedded within an anticyclonic vortex ring. *Geophysical Research Letters*, *45*, 7624–7633. https://doi.org/10.1029/2018GL077527

Ohlmann, J., Molemaker, M., Baschek, B., Holt, B., Marmorino, G., & Smith, G. (2017). Drifter observations of submesoscale flow kinematics in the coastal ocean. *Geophysical Research Letters*, *44*, 330–337. https://doi.org/10.1002/2016GL071537

Pasqueron de Fommervault, O., Perez-Brunius, P., Damien, P., Camacho-Ibar, V. F., & Sheinbaum, J. (2017). Temporal variability of chlorophyll distribution in the gulf of mexico: Bio-optical data from profiling floats. *Biogeosciences*, *14*(24), 5647–5662.

Poje, A. C., Özgökmen, T. M., Bogucki, D. J., & Kirwan, A. (2017). Evidence of a forward energy cascade and Kolmogorov self-similarity in submesoscale ocean surface drifter observations. *Physics of Fluids*, *29*(2), 020701. https://doi.org/10.1063/1.4974331

Portela, E., Tenreiro, M., Pallàs-Sanz, E., Meunier, T., Ruiz-Angulo, A., Sosa-Gutiérrez, R., & Cusí, S. (2018). Hydrography of the central and western gulf of mexico. *Journal of Geophysical Research: Oceans*, *123*(8), 5134–5149https://doi.org/10.1029/2018JC013813

Qiu, B., Chen, S., Klein, P., Wang, J., Torres, H., Fu, L.-L., & Menemenlis, D. (2018). Seasonality in transition scale from balanced to unbalanced motions in the world ocean. *Journal of Physical Oceanography*, *48*(3), 591–605. https://doi.org/10.1175/JPO-D-17-0169.1

Reffray, G., Bourdalle-Badie, R., & Calone, C. (2015). Modelling turbulent vertical mixing sensitivity using a 1-D version of NEMO. *Geoscientific Model Development*, *8*(1), 69–86. https://doi.org/10.5194/gmd-8-69-2015

Rudnick, D. L., & Cole, S. T. (2011). On sampling the ocean using underwater gliders. *Journal of Geophysical Research*, *116*, C08010. https://doi.org/10.1029/2010JC006849

Rudnick, D. L., Gopalakrishnan, G., & Cornuelle, B. D. (2015). Cyclonic eddies in the Gulf of Mexico: Observations by underwater gliders and simulations by numerical model. *Journal of Physical Oceanography*, *45*(1), 313–326. https://doi.org/10.1175/JPO-D-14-0138.1

Shcherbina, A. Y., D'Asaro, E. A., Lee, C. M., Klymak, J. M., Molemaker, M. J., & McWilliams, J. C. (2013). Statistics of vertical vorticity, divergence, and strain in a developed submesoscale turbulence field. *Geophysical Research Letters*, *40*, 4706–4711. https://doi.org/10.1002/grl.50919

Sosa-Gutiérrez, R., Pallàs-Sanz, E., Jouanno, J., Chaigneau, A., Candela, J., & Tenreiro, M. (2020). Erosion of the subsurface salinity maximum of the Loop Current Eddies from glider observations and a numerical model. *Journal of Geophysical Research: Oceans*, *125*, e2019JC015397. https://doi.org/10.1029/2019JC015397

Spall, M. A. (1995). Frontogenesis, subduction, and cross-front exchange at upper ocean fronts. *Journal of Geophysical Research*, *100*(C2), 2543–2557. https://doi.org/10.1029/94JC02860

Su, Z., Wang, J., Klein, P., Thompson, A. F., & Menemenlis, D. (2018). Ocean submesoscales as a key component of the global heat budget. *Nature Communications*, *9*(1), 1–8. https://doi.org/10.1038/s41467-018-02983-w

Taylor, J. R., & Ferrari, R. (2010). Buoyancy and wind-driven convection at mixed layer density fronts. *Journal of Physical Oceanography*, *40*(6), 1222–1242. https://doi.org/10.1175/2010JPO4365.1

Thomas, L. (2005). Destruction of potential vorticity by winds. *Journal of Physical Oceanography*, *35*(12), 2457–2466. https://doi.org/10.1175/JPO2830.1

Thomas, L., & Joyce, T. M. (2010). Subduction on the northern and southern flanks of the Gulf Stream. *Journal of Physical Oceanography*, *40*(2), 429–438. https://doi.org/10.1175/2009JPO4187.1

Thomas, L., & Lee, C. M. (2005). Intensification of ocean fronts by down-front winds. *Journal of Physical Oceanography*, *35*(6), 1086–1102. https://doi.org/10.1175/JPO2737.1

Thomas, L., Tandon, A., & Mahadevan, A. (2008). Submesoscale processes and dynamics. *Ocean Modeling in an Eddying Regime*, *177*, 17–38. https://doi.org/10.1029/177gm04

Thomas, L., & Taylor, J. (2010). Reduction of the usable wind-work on the general circulation by forced symmetric instability. *Geophysical Research Letters*, *37*, L18606. https://doi.org/10.1029/2010GL044680

Thomas, L., Taylor, J. R., Ferrari, R., & Joyce, T. M. (2013). Symmetric instability in the Gulf Stream. *Deep Sea Research Part II: Topical Studies in Oceanography*, *91*, 96–110. https://doi.org/10.1016/j.dsr2.2013.02.025

Thompson, A. F., Lazar, A., Buckingham, C., Garabato, A. C. N., Damerell, G. M., & Heywood, K. J. (2016). Open-ocean submesoscale motions: A full seasonal cycle of mixed layer instabilities from gliders. *Journal of Physical Oceanography*, *46*(4), 1285–1307. https://doi.org/10.1175/JPO-D-15-0170.1

Viglione, G. A., Thompson, A. F., Flexas, M. M., Sprintall, J., & Swart, S. (2018). Abrupt transitions in submesoscale structure in southern drake passage: Glider observations and model results. *Journal of Physical Oceanography*, *48*(9), 2011–2027. https://doi.org/10.1175/JPO-D-17-0192.1

Weatherly, G., Wienders, N., & Harkema, R. (2003). Temperature inversions in the open Gulf of Mexico. *Journal of Geophysical Research*, *108*(C6), 3177. https://doi.org/10.1029/2002JC001680

Wenegrat, J. O., Thomas, L., Gula, J., & McWilliams, J. C. (2018). Effects of the submesoscale on the potential vorticity budget of ocean mode waters. *Journal of Physical Oceanography*, *48*(9), 2141–2165. https://doi.org/10.1175/JPO-D-17-0219.1

Yang, Y., McWilliams, J. C., San Liang, X., Zhang, H., Weisberg, R. H., Liu, Y., & Menemenlis, D. (2021). Spatial and temporal characteristics of the submesoscale energetics in the Gulf of Mexico. *Journal of Physical Oceanography*, *51*(2), 475–489. https://doi.org/10.1175/JPO-D-20-0247.1

Yu, J., Zheng, Q., Jing, Z., Qi, Y., Zhang, S., & Xie, L. (2018). Satellite observations of sub-mesoscale vortex trains in the Western boundary of the South China Sea. *Journal of Marine Systems*, *183*, 56–62. https://doi.org/10.1016/j.jmarsys.2018.03.010

Yu, L. (2007). Global variations in oceanic evaporation (1958–2005): The role of the changing wind speed. *Journal of climate*, *20*(21), 5376–5390.

Yu, X., Naveira Garabato, A. C., Martin, A. P., & Marshall, D. P. (2021). The annual cycle of upper-ocean potential vorticity and its relationship to submesoscale instabilities. *Journal of Physical Oceanography*, *51*(2), 385–402. https://doi.org/10.1175/JPO-D-20-0099.1

Zavala-Hidalgo, J., Romero-Centeno, R., Mateos-Jasso, A., Morey, S. L., & Martínez-López, B. (2014). The response of the Gulf of Mexico to wind and heat flux forcing: What has been learned in recent years? *Atmósfera*, *27*(3), 317–334. https://doi.org/10.1016/S0187-6236(14)71119-1

Zhang, Z., & Qiu, B. (2018). Evolution of submesoscale ageostrophic motions through the life cycle of oceanic mesoscale eddies. *Geophysical Research Letters*, *45*, 11. https://doi.org/10.1029/2018GL080399

Zhong, Y., Bracco, A., Tian, J., Dong, J., Zhao, W., & Zhang, Z. (2017). Observed and simulated submesoscale vertical pump of an anticyclonic eddy in the South China Sea. *Scientific Reports*, *7*(1), 1–13. https://doi.org/10.1038/srep44011